

Multiscale mass transport in $z \sim 6$ galactic discs: fueling black holes.

Joaquin Prieto^{1*} & Andrés Escala¹

¹ *Departamento de Astronomía, Universidad de Chile, Casilla 36-D, Santiago, Chile.*

19 May 2022

ABSTRACT

By using AMR cosmological hydrodynamic N-body zoom-in simulations, with the RAMSES code, we studied the mass transport processes onto galactic nuclei from high redshift up to $z \sim 6$. Due to the large dynamical range of the simulations we were able to study the mass accretion process on scales from ~ 50 kpc to \sim pc. We studied the BH growth set on the galactic center in relation with the mass transport processes associated to both the Reynolds stress and the gravitational stress on the disc. Such methodology allowed us to identify the main mass transport process as a function of the scales of the problem. We found that in simulations that include radiative cooling and SNe feedback, the SMBH grows at the Eddington limit for some periods of time presenting a $\langle f_{\text{EDD}} \rangle \approx 0.5$ through out its evolution. The α parameter is dominated by the Reynolds term, α_R , with $\alpha_R \gg 1$. The gravitational part of the α parameter, α_G , has an increasing trend toward the galactic center, with values $\alpha_G \gtrsim 1$ at radii $\lesssim 10^2$ pc contributing to the BH fueling. In terms of torques, we also found that gravity has an increasing contribution toward the galactic center with pressure torques roughly dominating above $\sim 10^2$ pc. This complementary work between pressure gradients and gravitational potential gradients allows an efficient mass transport on the disc with an average mass accretion rates of the order $\sim 1 \text{ M}_\odot/\text{yr}$, which correspond to a fraction of $\sim 10^{-3}$ the average mass accretion rate at distances beyond the virial radius, a similar factor found in the BH - bulge mass scaling relation. This level of SMBH accretion rates found in our cosmological simulation are needed in all models of SMBH growth attempted to explain the formation of redshift 6 – 7 quasars.

Key words: galaxies: formation — large-scale structure of the universe — stars: formation — turbulence.

1 INTRODUCTION

The mass transport (MT) process on astrophysical environments has relevance on different phenomena in our Universe. It is important for the planet formation on proto-planetary discs, it trigger the AGN activity associated to super massive black holes (SMBH) accretion at high redshift and it is responsible for the mass accretion from the filamentary structure around dark matter (DM) haloes to the central region of the first galaxies. The full understanding of this phenomenon is very important in the construction of a galaxy formation theory.

In particular, the MT phenomenon has a crucial relevance in models of black holes (BH) formation and its growth at the early stages of our Universe. The observation of very bright quasars at redshift $z \gtrsim 6$ with luminosities $L \gtrsim 10^{13} L_\odot$ implies the existence of BH with masses of

the order $M_{\text{BH}} \sim 10^9 M_\odot$ when our Universe was about ~ 1 Gyr old (Fan et al. 2001), i.e. SMBH should be formed very early in the history of our Universe and they should grow very fast in order to reach such a high masses in the first $\sim \text{Gyr}$ of our Universe. To understand such a rapid early evolution is one of the main challenges of the current galaxy formation theories. For a more extended discussion on massive BH formation at high redshift see Volonteri (2010) and Haiman (2013).

There are three main scenarios for the formation of SMBH seeds:

- Seeds from the first generation of stars and its subsequent accretion to form the SMBH. Based on hydrogen molecular cooling simulations have shown that the first star would follow a top heavy initial mass function with masses in the range $\sim 10^2 - 10^3 M_\odot$ (Abel et al. 2002; Bromm & Larson 2004). Massive stars with masses above $\sim 260 M_\odot$ can

* email:joaquin.prieto.brito@gmail.com

leave a BH seed remnant of $\sim 100M_{\odot}$ (Heger & Woosley 2002).

- Massive seeds formed by the direct collapse of hot gas inside atomic cooling haloes. In this scenario the initial BH seeds are formed by the direct collapse of hot gas triggered by dynamical instabilities inside DM haloes of mass $\gtrsim 5 \times 10^7 M_{\odot}$ at high redshift, $z \gtrsim 10$ (e.g. Oh & Haiman (2002), Lodato & Natarajan (2006) and Begelman et al. (2006)). Such a process could form a BH seed of $\sim 10^4 - 10^6 M_{\odot}$, e.g. Begelman et al. (2008).

- BH seeds formed by dynamical effects of dense stellar systems like star clusters or galactic nuclei, e.g. Schneider et al. (2006). In this scenario the formed BH seed can be a mass $\sim 10^2 - 10^4 M_{\odot}$ (Devecchi & Volonteri 2009)

Studies related with the initial mass for the SMBH formation favor massive $\sim 10^4 - 10^6 M_{\odot}$ seeds inside primordial atomic cooling haloes (Volonteri et al. 2008; Tanaka & Haiman 2009; Lodato & Natarajan 2006).

There are dynamical evidence for the existence of SMBH in the center of nearby galaxies (Ferrarese & Ford 2005) with masses in the range $M_{BH} \sim 10^6 - 10^9 M_{\odot}$ suggesting that the BH formed at the first evolutionary stages of our Universe now are living in the galactic centers around us including our galaxy (Ghez et al. 2005). Beside their ubiquitous there are evidences of scaling relations connecting the BH mass with its host galaxy properties, namely the galactic bulge - BH mass relation (e.g. Gültekin et al. (2009)) and the bulge stars velocity dispersion - BH mass relation (e.g. Tremaine et al. (2002) and Ferrarese & Merritt (2000)). Such a relations suggest a co-evolution between the BH and its host galaxy.

Recent studies of galactic angular momentum (AM) acquisition and MT in a cosmological context have strength the relation between phenomena involving different scales in the Universe. These studies have shown a connection between the large scale structure and the rotational properties of DM haloes and galaxies now relating the filamentary structure of the cosmic web, which channelize most of the matter entering the halo virial sphere, with the galactic spins. In this work we will try to obtain some clues about how the matter transported by filaments can reach the central galactic region and feed the BH seed there at high redshift. Such phenomenon is tightly related with the AM transport process on galactic discs. In this sense we will not focus our attention to local phenomena around the BH but we will take into account the large scale dynamic of AM and MT.

In a cosmological context, motivated by the theoretical study of Pichon & Bernardeau (1999) a series of recent simulations Pichon et al. (2011) and Codis et al. (2012) have argued that the galactic spin may be generated entirely in the baryonic component due to the growth of eddies in the turbulence field generated by large-scales (\gtrsim few Mpc) mass in-fall. They found an interplay between both AM acquisition and MT on galactic scales with the big (\gtrsim few Mpc) cosmological scales. Such a finding is a clear motivation to study the potential connection between the cosmic web and the processes governing both the galaxy and BH evolution at high redshift.

Danovich et al. (2015) studied the AM acquisition process in galaxies at redshift $z \approx 4 - 1.5$ with a higher resolution simulations They separate the AM acquisition in 4

phases: i) the initial spin is acquired following the Tidal Torque Theory (Peebles 1969; Doroshkevich 1970) before the turn-around and transported to the DM halo through the filamentary structure of the cosmic web. ii) in this phase the mass and AM is transported to the halo outer region in the virialization process. Due to its coherent MT flows compared with the DM, the gas has a larger specific AM in this region; iii) in the disc vicinity the gas form a non-uniform ring which partially suffers the effect of the galactic disc torques producing an alignment with the inner disc AM; iv) finally, outflows reduce low specific AM gas increasing its global value at the central region and violent dynamical instabilities (VDI) associated to DM mergers and clump-clump interaction remove AM out allowing a more centrally concentrated gas.

At smaller scales (\sim few $100kpc$), Prieto et al. (2015) studied the MT and AM acquisition process in four DM haloes of similar mass $M \approx 10^9 M_{\odot}$ and very different spin parameter $\lambda = 0.001 - 0.04 - 0.06 - 0.1$ (Bullock et al. 2001a) at redshift $z = 9$. In this work they showed that before the turn-around the gas and DM AM are similar because they are feeling the same torques due to the inhomogeneous surrounded mass distribution (Peebles 1969; Doroshkevich 1970). After the turn-around the gas starts to feel the gas pressure implying that an additional source of torque works on the gas deviating its AM evolution from the DM AM. The pressure gradient continue increasing with the shell crossing ending with a decoupling between the gas AM and the DM spin vectors. Furthermore, they found a strong anti-correlation between the number of filaments converging onto the central DM halo and its spin parameter λ : the larger the number of filaments the lower the spin parameter. Such a finding relates the AM associated to mass accretion through filaments with the final spin of the small haloes, showing that in a cosmological context the MT process is not a local disc phenomenon but it relates scales including filaments of the cosmic web around the central DM halo until sub-virial scales associated to the disc surface. The anti-correlation found in the previous work suggests that SMBH would favor rare high density peaks places associated to knots of the cosmic web surrounded by a number of filaments. Under such a condition the accreted material would have to cross a lower centrifugal barrier to reach the central galactic region.

In a non-cosmological context, Escala (2006) and Escala (2007) has shown that the interplay and competition between BH feed and SF can naturally explain the $M_{BH} - \sigma$ relation. Using idealized isolated galaxy evolution simulations Bournaud et al. (2007) showed that $z \sim 1$ galaxies are able to form massive clumps due to gravitational instabilities (Toomre 1964) triggered by its high gas mass fraction (a common feature at high redshift due to the filamentary accretion from the cosmic web). Such a clumpy high redshift galaxies evolves due to VDI to form spiral galaxies characterized by a bulge and an exponential disc. They argue that due to the clump-clump interaction the disc material is able to migrate to the central galactic region and feed the potential BH in the center. Similar results have been found in cosmological contexts. By using cosmological hydrodynamical simulations Mandelker et al. (2014) shows that the formation of massive clumps is a common feature of $z \sim 3 - 1$ galaxies. The clumps are formed in place on the disc and

also are related to DM mergers. Due to the fast formation and interaction between them the VDI dominates the disc evolution. A similar clump migration has been observed at higher redshift in a $5 \times 10^{11} M_\odot$ DM halo at $z = 6$ in Dubois et al. (2012) and Dubois et al. (2013). In these works the migration has been triggered by DM merger induced torques.

Inspired by the α parametrization in the seminal paper of Shakura & Sunyaev (1973), Gammie (2001) studied the gravitational stability in cool thin discs characterized by a constant cooling time and showed that over a critical angular velocity the system can reach a steady-gravito-turbulent state. On the other hand, if the angular velocity is below this critical value the disc can fragment. In his work Gammie (2001) quantified the rate of angular momentum flux in terms of the Reynolds and gravitational stress. In this work we will use a similar α -formalism to study the MT process on galactic discs at redshift $z \sim 6$ performing N-body and hydrodynamic numerical simulations from cosmological initial conditions. We will study a halo of $\sim \text{few } 10^{10} M_\odot$, a mass value not studied already in this context. It is the first time that such an approach is being used to study the MT process on galaxies at high redshift. Furthermore we will compute directly the torques working on the simulated structures from ~ 50 kpc scales associated to the cosmic web around the central DM halo to $\sim \text{pc}$ scales associated to the galactic disc. Such an approach will allow us to have clues about the main source of mass transport on these objects and then to have some insights about the SMBH growth mechanisms at high redshift.

The paper is organized as follow. Section §2 contains the numerical details of our simulations. Here we describe the halo selection procedure, our refinement strategy and the gas physics included in our calculations. In section §3 we show our results. Here we present radial profiles of our systems, star formation properties of our galaxies, a gravitational stability analysis and show a mass transport analysis based on both the α formalism and the torques analysis on small and large scales. In section §4 we discuss our results and present our main conclusions.

2 METHODOLOGY AND NUMERICAL SIMULATION DETAILS

2.1 RAMSES code

The simulations presented in this work were performed with the cosmological N-body hydrodynamical code RAMSES (Teyssier 2002). This code has been written to study hydrodynamic and cosmological structure formation with high spatial resolution using the Adaptive Mesh Refinement (AMR) technique, with a tree-based data structure. The code solves the Euler equations with a gravitational term in an expanding universe using the second-order Godunov method (Piecewise Linear Method).

2.2 Cosmological parameters

Cosmological initial conditions were generated with the mp-grafic code (Prunet et al. 2008) inside a $L = 10$ cMpc side box. Cosmological parameters were taken from Planck

Collaboration (2013): $\Omega_m = 0.3175$, $\Omega_\Lambda = 0.6825$, $\Omega_b = 0.04899$, $h = 0.6711$, $\sigma_8 = 0.83$ and $n_s = 0.9624$.

2.3 Halo selection

Using the parameters mentioned above, we ran a number of DM-only simulations with $N_p = 256^3$ particles starting at $z_{ini} = 100$. We selected one DM halo of mass $M_{DM} \approx 3 \times 10^{10} M_\odot$ at redshift $z=6$. We gave preference to DM haloes without major mergers through its final evolution in order to have a more clean and not perturbed system to analyze.

After the selection process we re-simulated the halo including gas physics. For these simulations we re-centered the box in the DM halo position at redshift $z = 6$. These simulations were run using 3 DM nested grids filling the whole box. Each of these grids had 128^3 , 256^3 and 512^3 DM particles (covering the refinement levels from 7 to 9). Furthermore, we inserted another DM grid of 512^3 particles centered at the box central position covering $1/8$ of the total box volume (corresponding to refinement level 10). In this way we were able to reach a DM resolution equivalent to a 1024^3 particles grid inside the box central region, which corresponds to a particle mass resolution $m_{part} \approx 3 \times 10^4 M_\odot$, in other words we resolved the high redshift $\sim 10^6 M_\odot$ with $\gtrsim 30$ particles and our final halo with $\sim 10^6$ particles.

2.4 Refinement strategy

We follow a mask based refinement strategy. In other words, we allowed refinements inside the Lagrangian volume associated to a sphere of radius $R_{ref} = 3R_{vir}$ around the selected DM halo at $z_{end} = 6$. Such a Lagrangian volume is tracked back in time till the initial redshift of the simulation, $z_{ini}=100$. In this way we ensure that the simulation is resolving all the interesting volume of matter through out the experiment, i.e. all the material ending inside the R_{ref} at the end of the simulation.

In our simulations a cell is refined if one of the following conditions is fulfilled:

- it contains more than 8 DM particles,
- its baryonic content is 8 times higher than the average in the whole box,
- the local Jeans length is resolved by less than 4 cells (Truelove et al. 1997), and
- if the relative pressure variation between cells is larger than 2 (suitable for shocks associated to the virialization process and SNe explosions).

Following those criteria the maximum level of refinement was set at $\ell_{max} = 18$, corresponding to a co-moving maximum spatial resolution of $\Delta x_{min} \approx 38.1$ cpc and a proper spatial resolution of $\Delta x_{min} \approx 5.4$ pc at redshift $z = 6$. With this resolution we are able to resolve the inner $0.1R_{vir}$ DM region with ~ 200 computational cells.

2.5 Gas physics

Our simulations include optically thin gas cooling. The gas is able to cool due to H, He and metals following the Sutherland & Dopita (1993) model. The metals are modeled as passive scalars advected by the gas flow. In order to mimic the

effect of H_2 cooling in primordial environments all our simulations started with an initial metallicity $Z_{ini} = 0.001Z_\odot$ (Powell et al. 2011). This initial metallicity change through out one of our simulations due to SNe explosions. Furthermore, a uniform UV background is activated at $z_{reion} = 8.5$, following Haardt & Madau (1996).

2.5.1 Star formation

The numerical experiments include a density threshold Schmidt law for star formation: above a given number density, set to $n_0 = 10^4 \text{cm}^{-3}$ in our case (it is the typical number density at which the simulation reaches the higher level of refinement following the criteria mentioned above), the gas is converted into stars at a rate density, $\dot{\rho}_*$, given by

$$\dot{\rho}_* = \epsilon_* \frac{\rho}{t_{ff}(\rho)} \quad (1)$$

where ρ is the local gas density, $\epsilon_* = 0.05$ is the constant star formation efficiency and $t_{ff}(\rho)$ is the density dependent local free fall time of the gas¹.

When a cell reaches the conditions to form stars we create star particles following a Poisson distribution

$$P(N) = \frac{\lambda_P^N}{N!} e^{-\lambda_P}, \quad (4)$$

with N the number of formed stars and

$$\lambda_P = \frac{\rho \Delta x^3}{m_*} \frac{\Delta t}{t_*}, \quad (5)$$

where Δx is the cell grid side, $m_* \approx m_H n_0 \Delta x^3$ is the mass of the stars, assuming that it was formed in the highest level of refinement, Δt is the time step integration and $t_* = t_{ff}(\rho)/\epsilon_*$ is the star formation time scale. This processes end up with a population of stars inside the corresponding cell. In order to ensure numerical stability we do not allow to convert more than 50% of the gas into stars inside a cell.

2.5.2 SNe feedback

After 10 Myr the most massive stars explode as SNe. In this process a mass fraction $\eta_{SN} = 0.1$ of the stellar populations is converted into SNe ejecta:

$$m_{eject} = \eta_{SN} \times m_*. \quad (6)$$

In this case m_* is not the single stellar particle mass but the total stellar mass created inside a cell. Furthermore, each SNe explosion releases an specific energy $E_{SN} = 10^{51} \text{erg}/10M_\odot$ into the gas:

$$E_{eject} = \eta_{SN} \times m_* \times E_{SN}. \quad (7)$$

¹ In order to avoid numerical fragmentation we added a pressure floor to the hydrodynamical pressure. The pressure floor is computed as

$$P_{floor} = \frac{\rho k_B T_{floor}}{m_H \mu}, \quad (2)$$

with

$$\frac{T_{floor}}{\mu} = T_0 \left(\frac{n}{n_0} \right)^{\gamma_0 - 1}. \quad (3)$$

As mentioned above, metals are included as passive scalars after each SNe explosion and then they are advected by the gas flows. It means that after each SNe explosion a metallicity

$$Z_{eject} = 0.1Z_\odot \quad (8)$$

is included as metals to the gas in the simulation.

In this work we used the delayed cooling implementation of the SNe feedback (discussed in Teyssier et al. (2013); Dubois et al. (2015)). It means that in places where SNe explode the gas cooling is turned off for a time t_{diss} in order to take into account the unresolved chaotic turbulent energy source of the explosions.

As written in Dubois et al. (2015) the non thermal energy e_{NT} evolution associated to the SNe explosions can be expressed as

$$\frac{de_{NT}}{dt} = \eta_{SN} \dot{\rho}_* E_{SN} - \frac{e_{NT}}{t_{diss}} = \eta_{SN} \epsilon_* \rho \frac{E_{SN}}{t_{ff}} - \frac{e_{NT}}{t_{diss}}. \quad (9)$$

In an equilibrium state $de_{NT}/dt = 0$ it is possible to write

$$\frac{e_{SN}}{\rho} = \eta_{SN} \epsilon_* E_{SN} \frac{t_{diss}}{t_{ff}}. \quad (10)$$

If we assume that non thermal energy is associated to a turbulent motion with a velocity dispersion σ_{NT} and that this energy $e_{NT} = \rho \sigma_{NT}^2/2$ will be dissipated in a time scale of order the crossing time scale associated to the local jeans length then $t_{diss} \approx l_J/\sigma_{NT}$ it is possible to write

$$t_{diss} = \left(\frac{t_{ff}}{2\eta_{SN} E_{SN} \epsilon_*} \right)^{1/3} l_J^{2/3}. \quad (11)$$

Then, expressing the local Jeans length as $l_J = 4\Delta x$, with Δx the proper cell side at the highest level of refinement, it is possible to write the dissipation time scale as:

$$t_{diss} \approx 0.2[Myr] \left(\frac{0.1}{\eta_{SN}} \right)^{1/3} \left(\frac{0.05}{\epsilon_*} \right)^{1/3} \times \quad (12)$$

$$\left(\frac{\Delta x}{5.4[pc]} \right)^{2/3} \left(\frac{10^4[cm^{-3}]}{n_0} \right)^{1/6} \quad (13)$$

In our simulations this time will be of order \sim few 0.1 Myrs.

2.6 Sink particles and black hole accretion

In order to follow the evolution of a black hole (BH) in the simulations we introduced a sink particle (Bleuler & Teyssier 2014) at the gas density peak inside a DM halo of $M \approx 1.7 \times 10^8 M_\odot$ at redshift $z = 15.7$. The BH seed mass is $10^4 M_\odot$, roughly following the $M_{BH} - \sigma$ relation of McConell et al. (2011). We did not allow more BH formation after the formation of first one. In order to compute the mass accretion rate onto the BH we use the modified Bondi-Hoyle accretion rate described below.

2.6.1 Modified Bondi accretion

Bleuler & Teyssier (2014) implemented the modified Bondi mass accretion rate onto sink particles in the RAMSES code. They use the expression presented in Krumholz et al. (2004) based on the Bondi, Hoyle and Lyttleton theory (Bondi & Lyttleton 1939; Bondi 1952). There the Bondi radius

$$r_{BHL} = \frac{GM_{BH}}{(c_\infty^2 + v_\infty^2)} \quad (14)$$

defines the sphere of influence of the central massive object of mass M_{BH} and its corresponding accretion rate is given by

$$\dot{M}_{BHL} = 4\pi\rho_\infty r_{BHL}^2 (\lambda^2 c_\infty^2 + v_\infty^2)^{1/2} \quad (15)$$

where G is the gravitational constant, c_∞ is the average sound speed and v_∞ is the average gas velocity relative to the sink velocity, λ is an equation of state dependent variable and it is $\exp(3/2)/4 \approx 1.12$ in the isothermal case. The density ρ_∞ is the gas density far from the central mass and it is given by

$$\rho_\infty = \bar{\rho}/\alpha_{BHL}(\bar{r}/r_{BHL}) \quad (16)$$

where $\alpha_{BHL}(x)$ is the solution for the density profile in the Bondi model (Bondi 1952). The variable $x = \bar{r}/r_{BHL}$ is the dimensionless radius and $\bar{\rho}$ the corresponding density. In our case $\bar{r} = 2\Delta x_{min}$, with Δx_{min} the minimum cell size in the simulation.

The modified Bondi accretion rate is limited by the Eddington accretion rate. In other words, the sink particle can not accrete at a rate larger than the Eddington rate, given by:

$$\dot{M}_{Edd} = \frac{4\pi G m_p M_{BH}}{\sigma_T c \epsilon_r}, \quad (17)$$

where m_p is the proton mass, σ_T is the Thomson scattering cross section, c is the speed of light and $\epsilon_r = 0.1$ is the fraction of accreted mass converted into energy.

3 RESULTS

In this work we will analyze two simulations:

- NoSne simulation, it includes star formation and modified Bondi-Hoyle-Lyttleton (BHL) accretion rate onto sinks, and
- Sne simulation, it includes star formation, BHL accretion rate onto sinks and SNe feedback.

We are not including AGN feedback in these experiments, such an important ingredient has been left for a future study to be presented in an upcoming publication.

Figure 1 shows a gas number density projection of our systems at redshift $z = 6$. The left column contains the NoSne simulation and the right column the Sne simulation. The top rows show the large scale ($\sim 3 \times 10^2$ kpc) view of the systems and the bottom rows show a zoom-in of the central (~ 10 kpc) region.

In both top panels it is possible to recognize a filamentary structure converging on to the galaxy position. Such a filaments works as pipes channelizing cold baryonic matter onto the filaments converging region: the place for galaxy formation, i.e. knots of the cosmic web. Beside the accreted low density gas it is possible to recognize a number of overdensities associated to small DM haloes going to merger with the central dominant halo, a common feature of the hierarchical structure formation. Such a mini haloes certainly will perturb the galactic disc environment as we will see later.

Whereas at large scale we can note that the difference between both runs are the small scale features associated

to the shocks produced by SNe explosions on the top right panel, the bottom panels shows a clear difference between both simulations at the end of the experiments. The NoSne run developed a concentrated gas rich spiral galaxy whereas the Sne run has less gas available to form spiral arms and the dense gas looks much more spread on the volume showing a more extended spiral shape. Such a difference certainly is a consequence of SNe explosions (one of them has just exploded leaving the low density region in the bottom left panel): the injected energy into the environment is able to spread the gas out of the central region and then to decrease the average density due to effect of the SNe expanding bubbles. Such a phenomenon can destroy the galactic disc at higher z as we will show later. Furthermore, the metals release to the interstellar medium allow the gas to reach lower temperatures and create denser clumps. Figure 2 shows the rest frame face on stellar populations associated to our systems: NoSne run at the top panel and Sne run at the bottom panel. The images were made using three different filters from SDSS, namely u , V and i . There is no dust extinction.

Having this global picture in mind we will study the MT on high redshift $z \sim 6$ galaxies at multiple scales, from the filamentary structure around the DM central halo to the \sim pc scales associated to the local disc structure.

3.1 Radial profiles

Before to compute any surface or radial average from our AMR 3D data we aligned the gas spin vector with the Cartesian \hat{z} direction. After this procedure, we performed a mass weighted integration in the \hat{z} direction in order to have all the interesting physical quantities associated to the disc surface:

$$\langle Q(x, y) \rangle_z = \frac{\sum_{z_i}^{z_f} Q(x, y, z) \Delta m}{\sum_{z_i}^{z_f} \Delta m}, \quad (18)$$

with $\Delta m = \rho \Delta x^3$ and Δx the grid size.

In order to get our radial quantities we have performed a mass weighted integration in the cylindrical $\hat{\theta}$ direction to each of our disc surface data:

$$\langle Q(r) \rangle_z = \frac{\sum_{\theta=0}^{\theta=2\pi} Q(r, \theta) \Delta m}{\sum_{\theta=0}^{\theta=2\pi} \Delta m}, \quad (19)$$

where r and θ are the radial and azimuthal cylindrical coordinates, with $\Delta m = r \Delta r \Delta \theta$ and $\Delta r = \Delta x$.

Figure 3 shows the surface mass density of the gas (top panels), surface mass density of stars (central panel) and surface density star formation rate (bottom panel) for different redshifts as a function of radius. The left panel shows the NoSne results and the right panel the Sne results.

Both top panels show that the gas content of the central region tends to decrease with redshift. It means that the gas at the center of the galaxy has been consumed by both the star formation process and the accretion onto the BH (see the low density region at the galactic center in figure 1). It is worth to notice that in average the Sne run shows a lower surface mass density at high redshift compared with the NoSne. In this case the SNe explosions are able to spread out the gas on the DM central region. Such a process has a direct consequence on both the BH mass accretion rate

and the star formation rate as we will show in the following lines.

Both central panels show that the stars mass surface density increases monotonically with redshift. It is a manifestation of the conversion of gas into stars. Through out this process the large scale gravitational collapse channelizes the baryonic matter through filaments and then feeds the central DM halo region with cold material to be converted into stars. The mass density fluctuations in both components, stars and gas, are the evidence of the clumpy and not homogeneous nature of the gas in such high redshift environments: on one hand, the large scale gravitational collapse onto the central DM halo is able to generate shocks and turbulence on the galactic disc; such a turbulence are maintained in time for an additional source in our SNe run where the SNe explosions introduce more energy to the system and, on the other hand, the cold dense gas is able to form gravitationally bounded gas clumps on the disc as can be seen from figure 1.

As mentioned above, the bottom panels show the surface density star formation rate (SFR). In order to compute this quantity we took into account all the star with an age $t_* < 10$ Myr formed in the time elapsed between consecutive outputs. Furthermore, we took a maximum radius for the star mass integration as $r_{0.9} = 0.9 \times r_{\text{SF}}$, with r_{SF} the maximum radius at which there was recent star formation inside the DM virial radius, R_{vir} . The plots show an intermittent star formation process on the galactic disc for both runs.

The NoSne run shows a more equally distributed star formation process on the disc compared with the SNe simulation. Above the ~ 100 pc the SNe simulations shows star formation mainly at redshift from $z = 6$ to $z = 8$. In contrast, the NoSne disc shows features of star formation at all the sampled redshifts at ~ 100 . Such difference is related with the injection of energy associated to SNe explosions. This energy is able to quench the star formation in some regions of the disc reducing the local SFR (and sometimes destroying the galactic spiral shape). Furthermore, it is worth to notice that in the SNe run the explosions release metals to the primordial environment. In this case the metals increase the cooling rate of the gas allowing the disc to reach lower temperatures and then favor the collapse of new regions where SF can proceed. Such a process will work as a positive feedback for the SF process as we will show later (see also Powell et al. (2011) for example).

Figure 4 shows different gas velocities associated to our systems at different redshift as a function of radius. It plots the radial velocity $v_r \equiv \vec{v} \cdot \hat{r}$ (in solid blue line), azimuthal velocity $v_\theta \equiv \vec{v} \cdot \hat{\theta}$ (in long dashed cyan line) and the isothermal sound speed $c_s = (k_B T / \mu m_H)^{1/2}$ (in short dashed cyan line). The constants for the isothermal sound speed has the usual meaning: k_B is the Boltzmann's constant, T is the gas temperature, μ is the mean molecular weight and m_H is the proton mass.

In addition to the velocities mentioned above, we have computed the semi-Keplerian velocity v_{SKep} of the disc (in dotted orange line) and the turbulent rms velocity v_{rms} of the gas (in dot-dashed red line). These velocities are defined as:

$$v_{\text{SKep}} = \left(\frac{GM(< r)}{r} \right)^{1/2} \quad (20)$$

where G is the Newton's constant and $M(< r)$ is the total (gas, stars and DM) mass inside the radius r . The turbulent velocity is the radial average of

$$v_{\text{rms}} = [(v_r - \langle v_r \rangle)^2 + (v_\theta - \langle v_\theta \rangle)^2 + (v_z - \langle v_z \rangle)^2]^{1/2} \quad (21)$$

where $\langle v_{r,\theta,z} \rangle$ are the mean radial, rotational and z velocities, respectively.

In both simulations the radial velocity fluctuates from negative to positive values. Such a feature is a proof of a non stationary disc where at some radii there is inflowing material whereas at other radii there are gas outflows. Such a features can be produced by DM halo mergers or SNe explosions. It is worth to notice that at $r \gtrsim 1$ kpc, which correspond to the outer edge of the galactic disc, the gas is inflowing in most of the cases. Such a feature is a remarkable signal of fast radial gas inflows at distance $\sim 0.1 R_{\text{vir}}$ from the center of the system. These fast radial material comes from larger scales channelized by the filamentary structure shown in the top panels of figure 1 and, as mentioned above, they supply the central DM halo region with cold gas at rates as high as $\sim 10 [M_\odot / \text{yr}]$ as we will see in the following sections sections. In other words, these systems tend to have a non negligible radial velocity at the galactic edge.

The orbital velocity tends to be roughly similar to the semi-Keplerian one at large radii $r \gtrsim 100$ pc in most of the cases but in general the circular velocity does not follow the semi-Keplerian orbit. Such a deviations from the smooth semi-Keplerian curve can be explained due to the strong-shocked gas inflows, the mergers suffered by the central halo which perturb the gas and by SNe explosions. We strength that these kind of interaction have a gravitational effect due to tidal forces on the disc and also have a hydrodynamical effect due to the shocks produced by the mergers and SNes. In our SNe run it is clear that the semi-Keplerian curves are lower than the NoSne curves. In other words the enclosed mass inside $\sim 0.1 R_{\text{vir}}$ is lower in the SNe run. That is because the SNe explosions spread the gas out of the central region. Actually from the shocked gas features at the top right panel of figure 1 it is possible that the outflows can reach regions at ~ 100 ckpc from the central galaxy, i.e. ~ 15 kpc at $z = 6$.

For all redshifts the sound speed is no more than \sim few 10 km/s. It means that the sound speed is much lower than the turbulent rms velocity of the gas. In other words, the gas on the disc is turbulent with a Mach number of order \sim few 10. In summary, the large scale gravitational collapse, SNe explosions and mergers events work together to create a high Mach number turbulent gas disc. Under such a dynamical conditions we will analyze the MT process on high redshift galaxies.

3.2 Kennicutt-Schmidt law

Despite of there is not observations of the Kennicutt-Schmidt (KS) law at high redshift ($z \gtrsim 6$) it is interesting to compare the KS law from our simulations with its current accepted functional form (Kennicutt 1998):

$$\dot{\Sigma}_* = (2.5 \pm 0.7) \times 10^{-4} \left(\frac{\Sigma_{\text{gas}}}{1 M_{\odot}/\text{pc}^2} \right)^{1.4} [M_{\odot}/\text{yr}/\text{kpc}^2] \quad (22)$$

Figure 5 shows the KS law for both runs: NoSne at top and Sne at bottom. Each point marks the surface density star formation rate as a function of the gas surface density. The point color marks the redshift of the calculation: the dark ones mark low redshift and the light ones mark high redshift. The black solid line marks the functional form of the KS law.

In our two runs the data coincides with the expected Kennicutt (1998) relation, in other words our simulations are producing stars at a roughly similar rate compared with the observed rate in the local Universe.

The main difference between our experiments are: First, we see that the Sne simulation reaches higher surface densities on the disc. It is possible due to the enhanced cooling associated to the metals released to the environment after SNe explosions and due to the gas compression associated to the expanding SNe bubbles. Beside the negative feedback of SNe heating on SF the enhanced cooling due to metals allows the gas to reach lower temperatures and then favor the SF process, as we will see below. Due to the low metallicity it is not possible to observe such effect on the NoSne run. In this experiment the gas is constantly consumed and there is not an additional process to drop the gas temperature, then the gas can not reach higher densities. The second difference that we can see is the data dispersion at low redshift $z \lesssim 7$. The low redshift point in the NoSne experiment have a larger dispersion (~ 2 dex) compared with the SNe ones (~ 1 dex). In other words, at low redshift the Sne run tends to be closer to the KS law than the NoSne run.

As a complementary analysis it is illustrative to compute the stellar metallicity evolution of our Sne run, the total stellar mass evolution of our systems and their total SFR.

Figure 6 shows the mass weighted average of the stellar metallicity as a function of redshift for our Sne experiment. The solid blue line marks the stellar metallicity inside the virial radius and the cyan dashed line marks the central stellar metallicity inside $0.1R_{\text{vir}}$. The stellar metallicity grows from $Z \sim 10^{-3} Z_{\odot}$ at $z = 15$ to $Z \sim 10^{-1} Z_{\odot}$ at the end of the experiment. It grows almost monotonically with redshift and the central metallicity tends to be slightly higher than the metallicity inside the virial radius. In other words, the stars in the central region are more metal rich because they tend to be formed on the stellar disc from enriched material whereas the average inside the virial radius can include stars formed in more metal poor regions in principle not necessarily associated with the central galactic disc.

Figure 7 shows the stellar mass normalized by the $f_b M_{\text{vir}}$, where $f_b \equiv \Omega_b/\Omega_m$ is the universal baryonic fraction. The filled circles marks the stellar mass inside the virial radius and the empty triangles the stellar mass inside $0.1R_{\text{vir}}$. The difference between these two computations is not too much in both runs and at some redshift both values are almost the same showing that most of the stellar content of the DM halo is inside one tenth of its virial radius. The NoSne run (top panel) forms more stars compared with the Sne run (bottom panel). Such a difference is a clear signal of the regulation of SF due to SNe explosions. The SNe energy injection reduce the final stellar mass to one half in the Sne run compared with the NoSne experiment. It is worth

to notice that our results are in good agreement with the one obtained Kimm et al. (2015) for their thermal feedback simulations (see the cyan triangles of their figure 8).

Figure 8 shows the SFR for both runs as a function of redshift: without SNe feedback (solid blue line) and with SNe feedback (dashed cyan line). It is worth to notice that both runs show a different SFR. The NoSne run shows a roughly constant SFR below $z \sim 13$ with values \sim few M_{\odot}/yr till $z \sim 7$ and in contrast the Sne run shows increasing peaks of SFR with huge fluctuations associated to bursts of star formation. In this case the SFR is practically null at some redshifts due to the SNe injection energy which, as we can see, is able to stop the SF process. Below $z \sim 9$ the NoSne SFR is higher, but below this redshift the Sne run shows higher peaks. In this sense, we can say that at high redshift $z \gtrsim 9$ the SNe feedback produces significant drops in the SFR but below this redshift multiple processes like, the enhanced cooling associated to the metals, the higher gas fraction and the deeper gravitational potential well allow the gas to produce star at a higher rate compared with the NoSne experiment. Here we again compare our results with the thermal feedback run of Kimm et al. (2015) and found a good agreement between them (see the dotted cyan line of the right panel of their figure 5).

3.3 Disc stability

High redshift galactic environments have a high gas fraction due to the very efficient filamentary accretion on DM haloes. Figure 9 shows the gas fraction of our systems as a function of redshift. Here we define the gas fraction as the ratio between the gas content and the gas plus the DM content inside a given radius: $M_{\text{gas}}/(M_{\text{gas}} + M_{\text{DM}})$. Both systems shows a high gas fraction inside $0.1R_{\text{vir}}$. The gas fraction can be as high as $\sim 30\%$ in the inner halo region. Despite the SNe can produce a gas depletion for some periods decreasing the amount of gas in the galaxy the almost continuous filamentary injection of cold gas allows the system to recover its high gas fraction. We do not include the mass of the stars in this calculation which is a negligible fraction $\lesssim 10^{-1}$ of the total baryonic content.

The non-stationary and highly dynamic nature of the systems makes them susceptible to a gravitational instabilities. In order to analyze the disc stability through out its evolution we will use the Toomre parameter, Q_T , stability criterion (Toomre 1964):

$$Q_T = \frac{c_s \Omega}{\pi G \Sigma} \quad (23)$$

Figure 10 shows the Toomre parameter for our two runs at different redshifts: $z = 6$ in solid blue line, $z = 7$ in long dashed cyan line, $z = 8$ in short dashed green line, $z = 9$ in dotted orange line and $z = 10$ in dot-dashed red line. The gray dashed horizontal line marks the $Q_T = 1$ state.

Both runs show a mixed behavior of unstable $Q_T < 1$, marginally stable $Q_T \approx 1$ and stable regions $Q_T > 1$. It is clear that the stabilizing effect of SNe heating works on the Sne run galactic disc. In this experiment the Q_T parameter tend to be $\gtrsim 1$ at all the shown redshift for radii \gtrsim few 10 pc. Only at $z = 10$ and $z = 7$ the central regio seems to be unstable in this case. On the other hand, the NoSne run shows much more unstable regions between few ~ 10

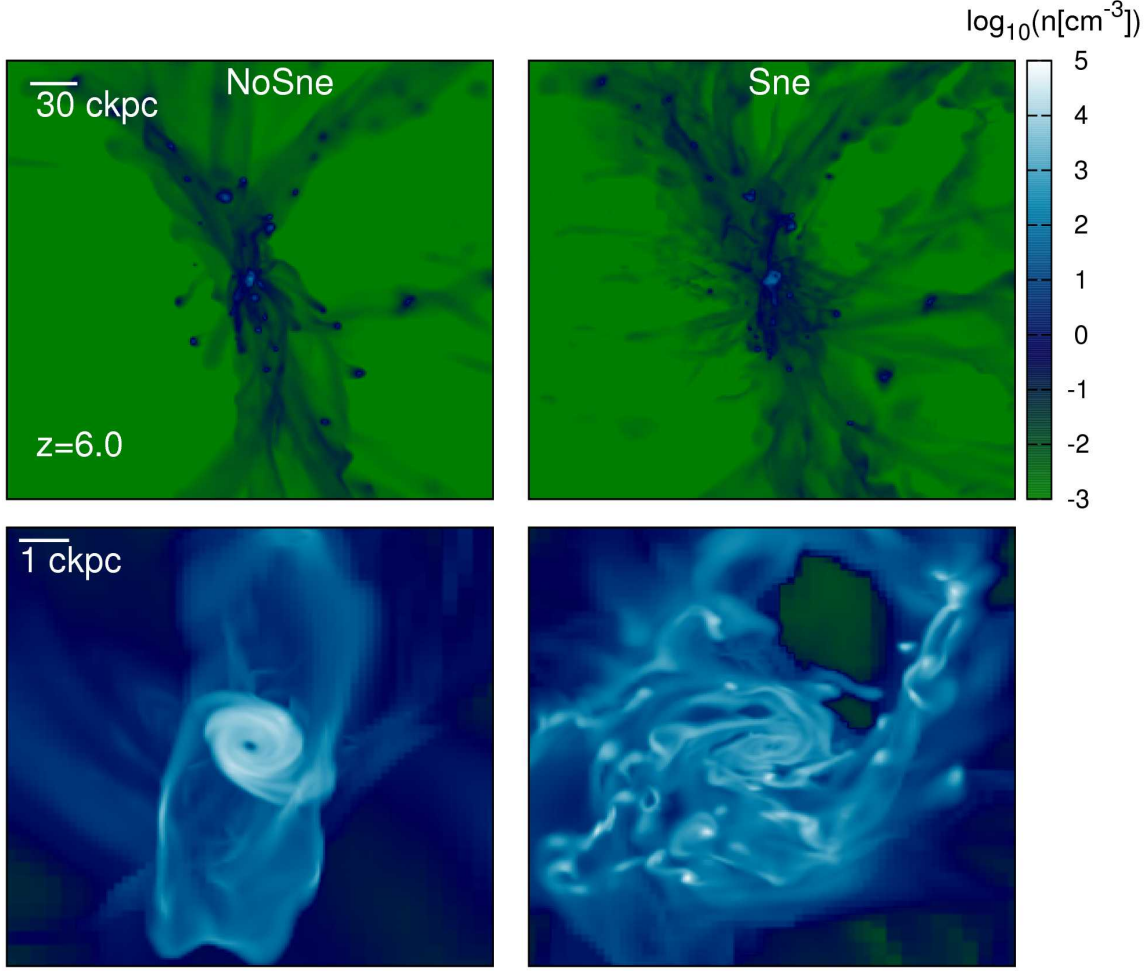


Figure 1. Mass weighted projection of the gas number density for both simulations: NoSne left column and Sne right column. The top row is a large scale (~ 300 ckpc square side) of our systems and the bottom row is a zoom-in of the central region of the system (~ 10 ckpc square side). From both top panels it is possible to identify the filamentary structure converging at the central region of the system: the galaxy position. Such a filaments channelize and feed the galactic structure. At large scales it is possible to recognize shock waves associated to the SNe explosions of our Sne run. Beside the low density gas, there is a number of over-densities associated to small DM haloes going to merge with the central structure. The bottom panels show a dramatic difference between our simulations: a compact gas rich spiral galaxy for the NoSne experiment and, on the other hand, a much more disturbed and extended galaxy with a number of clumps and a lower average density for our Sne run.

pc to few ~ 100 pc at $z \gtrsim 7$. Furthermore, almost at all redshifts it is possible to see unstable gas at the galactic center. It is interesting to note that at $\sim 0.1R_{vir} \lesssim 1$ kpc the gas is gravitationally stable showing a $Q_T \gg 1$. This fact is consistent with a definition of the galactic disc edge at $\sim 0.1R_{vir}$.

Figure 11 shows the mass associated to the maximum unstable scale length on rotating disc (Escala & Larson 2008)

$$M_{cl}^{max} = \frac{\pi^4 G^2 \Sigma_{gas}^3}{4\Omega^4} \quad (24)$$

The above expression has a strong dependence on Σ_{gas} , so we can anticipate that M_{cl}^{max} will have huge fluctuations in clumpy discs. The figure shows the maximum mass for the NoSne run at the top panel and for the Sne run at the bottom panel for different redshifts as a function of radius. We have plotted the radial dependence starting from 10 pc

because it is of the order of typical values for the turbulent disc scale height at a few pc from the center.

It is worth to notice that at radii above ~ 100 pc the mass scale has a floor of $\sim 10^4 M_\odot$ with huge fluctuations due to the mass clumps on the disc for both experiments. Beside the mass floor we can see that in general the maximum mass tend to be of the order of $\sim 10^6 M_\odot$ on the galactic disc.

We applied the clump finder algorithm of Padoan et al. (2007) to our galactic disc. The clump finder algorithm scans regions of density above $10^3 n_{avg}$, with n_{avg} the average density inside the analyzed box. In practice it means that we look for gas clumps at densities above $\sim 5 \times 10^3 \text{ cm}^{-3}$. The scan is done increasing the density by a fraction $\delta n/n = 0.25$ till the maximum box density. For each step the algorithm selects the over-densities with masses above the Bonnor-Ebert mass in order to define a gas clump. The previous algorithm gave us clump masses in the range

$\sim 10^5 - 10^8 M_\odot$ in good agreement with the theoretical expectation of M_{cl}^{max} .

3.4 Mass transport on the disc

It is well known that in a cosmological context the large scale ($\gtrsim R_{vir}$) gas cooling flows associated to DM filaments converging onto DM haloes have influence on the small scales ($\lesssim R_{vir}$) galactic AM (Prieto et al. 2015; Danovich et al. 2015; Powell et al. 2011). Such an interplay between large and small scales suggests that the mass/AM transport analysis should be performed taking into account both regimes. In the next subsections we will analyze the MT process taking into account the large scale filamentary accretion and the small scale mass fluxes on the galactic disc.

3.4.1 Stresses on the disc

The MT on the galactic disc can be studied based on the momentum conservation equation. Written in its conservative form this equation tell us that the local variation of momentum is due to the rate of momentum flux:

$$\frac{\partial(\rho v_i)}{\partial t} + \frac{\partial}{\partial x_k}(R_{ik} + P_{ik} - G_{ik}) = 0, \quad (25)$$

where ρ is the gas density, x_i are the Cartesian coordinates and v_i are the Cartesian components of the gas velocity. All the terms inside the divergence are by definition rates of momentum flux and they can be written as follow.

$$R_{ik} = \rho v_i v_k. \quad (26)$$

is the Reynolds (or hydrodynamic) stress and it is related to the inertial motion of the fluid. Instead of to be a source of momentum flux it quantifies the transported momentum due to the addition of different phenomena on the disc, namely gravitational stresses, magnetic stresses, viscous stresses or pressure stresses.

$$P_{ik} = \delta_{ik} P. \quad (27)$$

Is the pressure stress, where P is the gas pressure and its gradient will be a source torque as we will show in the following lines.

$$G_{ik} = \frac{1}{4\pi G} \left[\frac{\partial \phi}{\partial x_i} \frac{\partial \phi}{\partial x_k} - \frac{1}{2} (\nabla \phi)^2 \delta_{ik} \right]. \quad (28)$$

with ϕ the gravitational potential, G the Newton's constant and δ_{ik} the Kronecker delta symbol. G_{ik} is the gravitational stress and it is related with the movements of the fluid due to the gravitational acceleration. This term also will be a source of torques acting on the fluid as we will show in the next lines.

Because we are not including magnetic fields we ruled out the term associated to it. Furthermore, the dissipative-viscous term is negligible in this context and will not be taken into account in the following discussion (Balbus 2003).

On the disc MT context it is useful to quantify the momentum transport in the \hat{r} direction due to processes in the $\hat{\theta}$ direction where \hat{r} and $\hat{\theta}$ are the radial and the azimuthal cylindrical coordinates, respectively. If $F_{r\theta}$ is the rate of momentum flux in the \hat{r} direction due to the processes in the $\hat{\theta}$ direction associated to any of the stresses mentioned above, in general we can write (see the appendix A)

$$F_{r\theta} = \frac{1}{2}(F_{yy} - F_{xx}) \sin 2\theta + F_{xy} \cos 2\theta. \quad (29)$$

It is interesting to note that this term can also be interpreted as the change of $\hat{\theta}$ AM due to fluxes in the \hat{r} direction.

After some algebra it is possible to write the momentum fluxes for each of our sources as follow (e.g. Balbus (2003) and Fromang et al. (2004) and references therein):

$$R_{r\theta} = \rho(\vec{v} \cdot \hat{r})(\vec{v} \cdot \hat{\theta}) \quad (30)$$

$$P_{r\theta} = 0 \quad (31)$$

$$G_{r\theta} = \frac{1}{4\pi G} (\nabla \phi \cdot \hat{r})(\nabla \phi \cdot \hat{\theta}) \quad (32)$$

It is worth to notice that in case of θ symmetry the gravitational term vanishes. In other words, any density perturbation in the $\hat{\theta}$ direction, e.g. an asymmetric gas clumps distribution on the disc, will cause a momentum flux in the \hat{r} direction. This will be the term associated to the VDI as we will show later.

In this context it is useful to define an α parameter for each of our stresses. For a given rate of momentum flux, following Gammie (2001), we define:

$$\alpha_{r\theta} = \alpha_{R,r\theta} + \alpha_{G,r\theta} = \frac{R_{r\theta} + G_{r\theta}}{P} \quad (33)$$

Each α parameter is interpreted as the rate of momentum flux associated with a given process normalized by the gas pressure. Because the gas pressure is $P \sim (\rho c_s) \times c_s$ it can be interpreted as a “thermal momentum” advected at the sound speed or as a “thermal rate of momentum flux”. In this sense an $\alpha \gtrsim 1$ is a sign of super-sonic movements on the fluid. This parameter is $\alpha \approx 0.02$ for ionized and magnetized discs (Fromang et al. 2004; Nelsen & Papaloizou 2003) and observations of proto-stellar accretion discs (Hartmann et al. 1998) and optical variability of AGN (Starling et al. 2004) give an alpha parameter ~ 0.01 .

Figure 12 shows the radial values of $\alpha_{R,r\theta}$ in the top row and $\alpha_{G,r\theta}$ in the bottom row for the NoSne simulation at the left column and the Sne run at the right column for different redshifts.

The first thing that we should notice from this figure is that the α parameters are not constant neither in time nor in space and furthermore they reach values above unity. In other words, our high redshift galactic discs are not in a steady state. Such a dynamical condition does not allow to use the Shakura & Sunyaev (1973) mass accretion rate expression as a function of the computed α parameter. (See appendix B for a more detailed discussion.) Instead of that we must compute a mass accretion rate directly from our data.

From the figure it is clear that the Reynolds stress is much larger than the gravitational stress and then it dominates the MT process (note that both top and bottom panels are not in the same α range). In other words, the rate of momentum flux associated to the gravitational potential gradients is lower than the rate of momentum flux associated to the bulk motion of the gas. The gravitational stress can be compared to the lowest Reynolds stress values only at the inner most region of the system, it means that at the disc central region the gravitational potential gradient are more important than in other regions of the disc.

Here we emphasize that the Reynolds tensor is not a source of momentum flux, in the sense that if we start the

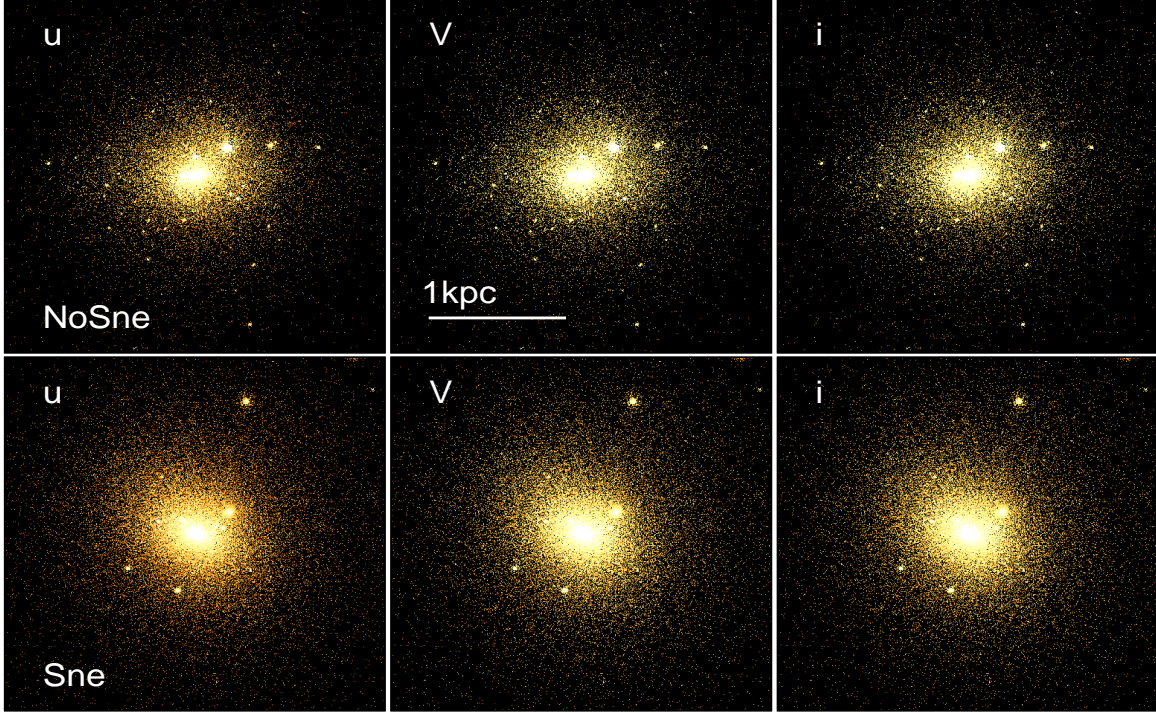


Figure 2. Rest frame stars visualization for the NoSne run in the top row and for the Sne run in the bottom row for three different filters from SSDS: u at the left panels, V at the central panel and at the i panel. The images correspond to the end of our simulations and there is not dust extinction.

disc evolution from a semi-Keplerian rotation state, i.e. without a radial velocity component, with null viscosity and one small gravitational potential perturbation in the θ direction the variation in momentum will be associated to the gravitational stress and the appearance of the Reynolds stress will be a consequence of this process.

It is interesting to note that the $\alpha_{G,r\theta}$ parameter in both experiments have a decreasing trend with the galactic radius: the smaller the radius the larger the gravitational stresses. If we take into account that the accreted material tends to concentrate in the inner part of the galaxy then it is reasonable that the larger gravitational stresses act at small radii. In the NoSne run it is of the order of pressure at the galactic center at all redshifts, whereas in the Sne run it is well above the pressure at $z = 6$ as we can see from the $\alpha = 1$ gray dashed line.

We can see that the Sne simulation shows slightly higher peaks in the Reynolds stress compared with the NoSne run. The SNe explosions can explain the difference between them in our experiments. Taking into account that the Reynolds stress depends on the gas velocity, it is clear that if there is any source of energy increasing the fluid velocity it will have a direct impact on the values of $\alpha_{R,r\theta}$. In this case the source of energy are the SNe explosions and the result is a higher alpha parameter associated to the bulk motion of the gas for the Sne experiment.

As the α parameter measures the importance of the stresses compared with the gas pressure we can say that the rate of momentum flux associated to the bulk motion is much larger than the gas pressure and the gas pressure dominates over the gravitational stress at scales $r \gtrsim 50$ pc at high redshift $z \gtrsim 8$. Only at small radius and at low redshift the gravitational rate of momentum flux can dominate (in the Sne case) over the gas pressure. Those facts will be relevant when we compare the torques associated to the gravity and pressure in the following sub sections.

3.4.2 Time scales

It is interesting to take a look on the time scales involved in this physical phenomenon. Based on the dynamic of the system we can define the radial, t_{rad} and the orbital, t_{orb} time scale at a given radius of the disc. Such a time scales can be compared between them and with the local free fall time at a given distance from the galactic center to have an idea of how fast is the gas falling onto the galaxy and how fast the gas is rotating around the galactic center. Then we define

$$t_{rad} = \frac{r}{v_r}, \quad t_{orb} = \frac{2\pi r}{v_t} \quad \text{and} \quad t_{ff} = \left(\frac{3\pi}{32G\rho} \right)^{1/2}. \quad (34)$$

Figure 13 shows the ratio between the radial and the orbital time in solid blue line and the ratio between the

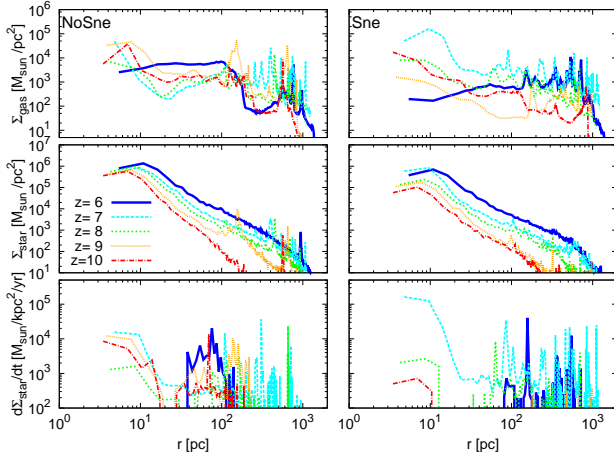


Figure 3. Radial profiles of the surface gas mass density (top panels), surface star mass density (central panel) and surface star formation rate (bottom panel) for the NoSne run in the left column and the Sne run in the right column. All the quantities are plotted for different redshifts: $z = 6$ in solid blue line, $z = 7$ in long-dashed cyan line, $z = 8$ in short-dashed green line, $z = 9$ in orange dotted line and $z = 10$ in dot-dashed red line. The top and central panels show density fluctuations associated to the non homogeneous nature of the galactic disc at high redshift. The top left panel shows that the gas surface density in the Sne case is lower than in the NoSne case. In fact, SNe explosions are able to deplete the gas from the galaxy at high z . Both central panel shows a monotonic increment with z , a manifestation of the conversion of gas into stars. The bottom panels show low surface SFR at intermediate radii compared with the NoSne. Certainly the difference is due to the SNe thermal feedback on the gas.

radial and the free-fall time in dashed cyan line as a function of radius for both simulations: NoSne at the left column and Sne at the right column. The ratios were computed for different redshifts: $z = 6$ at the top panel, $z = 8$ at the central panel and $z = 10$ at the bottom panel. The gray dashed line marks the ratio equal to 1.

At the edge of the galactic disc, $r \gtrsim 1\text{kpc}$ the radial time is similar to the free fall time (cyan dashed line) for most of the redshifts shown in the figure. In order to understand that we have to take into account the large scale filamentary structure surrounding our systems: as a result of the gravitational collapse of the baryonic matter through filaments onto the central DM halo the gas is able to free fall roughly until the last kpc ($\sim 0.1R_{\text{vir}}$). Such a feature is responsible of the high gas fraction of the systems. At lower radii this ratio starts to increase. In fact, when the material tries to flow to the inner parts of the disc it starts to feel the pressure of the accumulated gas at the last tenth of the virial radius. Certainly this process will stop its free-fall reducing its velocity.

The radial to orbital time ratio (solid blue line) fluctuates above and below the gray dashed line. The radial time scale some times is higher and other it is lower than the orbital time. Such a behavior shows the presence of fast radial flows on the disc: the gas can flow to the center in times shorter than the orbital time. In contrast to the evolution of an isolated stationary disc, in a cosmological context the cooling flows associated to the DM filaments and the DM

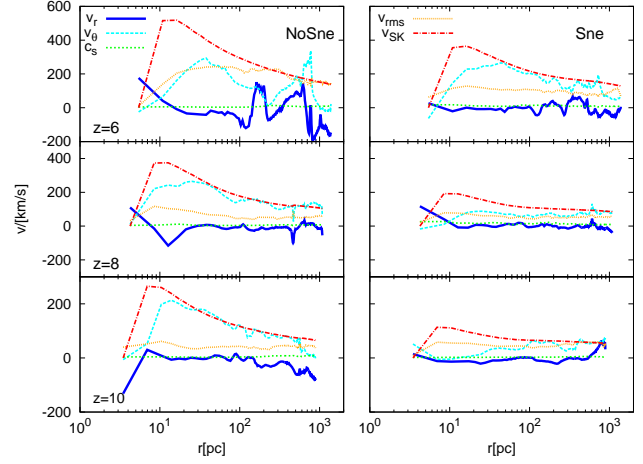


Figure 4. The figure shows the gas radial velocity (in solid blue line), orbital velocity (in long-dashed cyan line), sound speed (short-dashed green line), turbulent rms velocity (in dotted orange line) and the semi-Keplerian velocity (in dot-dashed red line) as a function of radius at different redshifts for the NoSne run (left columns) and the Sne run (right column). The disc shows fast radial inflows at large radii ($r \gtrsim 1\text{ kpc}$, i.e. the edge of the galactic disc) due to the large scale gravitational collapse. Strong gas inflows, DM halo mergers and SNe explosions create a turbulent environment with Mach numbers of order $\sim \text{few } 10$. Such a violent process is able to deviate the gas from semi-Keplerian orbits on the disc.

mergers are very efficient transporting material from large scales to the small galactic scales, as can be seen from these results. In this sense, such a high radial velocities are not a surprise and they can explain the high α_R found in the previous sub section.

3.4.3 Torques on the disc

After to observe that the Reynolds stress associated to the gas inertial motion dominates the rate of momentum flux on the disc and that the gravitational α reaches its maximum at the central galactic region, it is relevant for the MT study to analyze the torques acting on the disc. In order to do that we compute the torques associated to both the gravity and the gas pressure for our systems. We define these two quantities as:

$$\vec{\tau}_G = \vec{r} \times \nabla \phi, \quad (35)$$

$$\vec{\tau}_P = \vec{r} \times \frac{\nabla P}{\rho} \quad (36)$$

which actually are specific torques, i.e. torques per unit gas density. These two terms will act as source of AM transport on the galactic disc and will give us some clues about the MT process on high redshifts galactic discs.

Figure 14 shows the gravitational torque at the top panels for both the NoSne and the Sne run, the pressure torque at the middle panel and the modulus of the ratio of these two quantities at the bottom panel at the different redshifts as a function of galactic radius. The first two rows are associated to the torques producing an inward MT.

From the first row we can see that the gravitational torques have a huge scatter and there is not clear trend

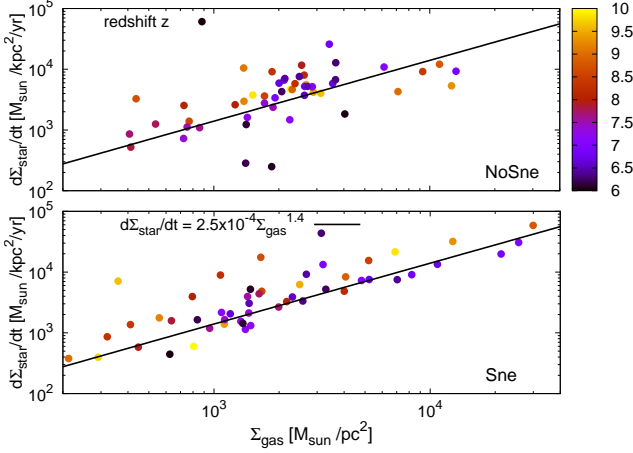


Figure 5. KS law for each of our snapshots from $z = 10$ to $z = 6$. Each point marks the KS relation for our disc computed as mentioned in the text at different redshifts in different colors. The NoSne run shows a larger data dispersion compared with the Sne run. Furthermore it is possible to see that the Sne run follows better the relation at low redshift (dark points).

in radius. Such a fluctuations reflect the complex density structures on the disc. It is possible to see that our Sne run has slightly lower values compared with the NoSne, such a difference is related with lower average gas density in this simulation due to the SNe energy injection which tends to spread the gas out on the disc. The picture changes when we look at the pressure torques. For the NoSne run it is possible to see an increasing trend with the radius. At the edge of the disc the pressure torques are more important than at the inner part of the disc. Here we have to note again that at the outer disc region there is an interaction layer between the galactic disc gas and the material free falling onto the DM central region from the large scale cosmic web. Such a violent interaction layer certainly will have an additional effect on the torques beside the radial scaling of it (as was shown in figure 12). On the other hand, the Sne run does not present the same clarity in the trend, but still we can see a rough decreasing trend. In this case the pressure torques show more dispersion with higher values on the disc at some redshifts. Clearly, such a huge dispersion is due to the SNe events injecting energy which produces a large pressure gradient on the disc.

The bottom panels of figure 14 show the ratio between τ_G and τ_P , with $\tau_i \equiv |\vec{\tau}_i|$. Both runs show a roughly decreasing trend, due to the increasing trend of the pressure torque. Beside the rough decreasing trend which means that pressure tends to dominate at the galactic edge-external regions, $r \gtrsim 100$ pc, and gravity tends to dominate at the galactic central region, $r \lesssim 100$ pc, the NoSne run shows that the torques ratio fluctuates around 1 implying a mixed contribution from both source of torques. A similar picture can be seen from the Sne experiment results. There it is also possible to see a decreasing trend with radius, but in this case the points tends to be below the $\tau_G/\tau_P = 1$ line. Despite of that, there are a number of regions where the gravity torques dominate on the disc. Again, as in the NoSne case, we can see a mixed behavior: pressure and gravitational torques work

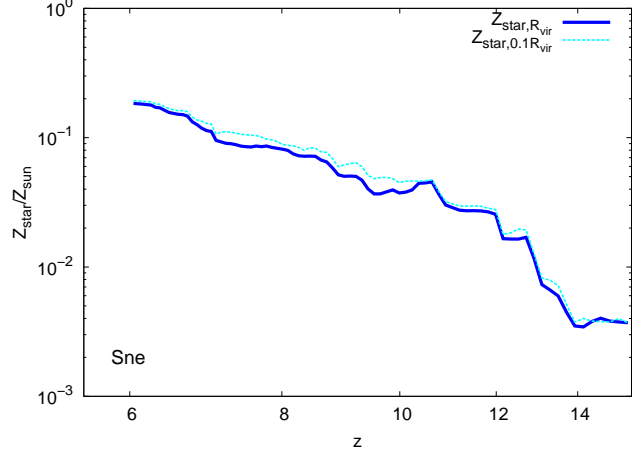


Figure 6. Stars metallicity evolution for our SNe experiment as a function of redshift. The solid blue line marks the stars metallicity inside the virial radius of the system and the cyan dashed line marks the stars metallicity inside one tenth on the virial radius. The cyan dashed line tends to be slightly above the blue solid line showing a more metal rich environment in the central halo region.

together on the high z galactic disc with gravity dominating the central $r \lesssim 100$ pc regions fueling the BH and pressure dominating the outer $r \gtrsim 100$ pc region. This conclusion is in agreement with our previous results on the α parameters analysis.

As a complement to our findings it is useful to take a look on torques at large scales. Figure 15 shows the ratio of the total torques (not only the \hat{z} component on the disc) τ_G/τ_P for both runs: NoSne in the left column and the Sne to the right column, and for two different redshifts, $z = 10$ in the top row and $z = 6$ in the bottom row. Each panel has an area of $\sim 600^2$ ckpc². The maps take into account the gas with density above $50 \times \Omega_b \rho_c / \Omega_m$, where ρ_c is the critical density of the Universe. Such a cut in density was set by inspection in order to have a clear view of the filaments around the central DM halo.

It is interesting to note that in both simulations the border of the filaments is clearly dominated by the pressure torque: material from voids falls onto the filamentary DM structure creating large pressure gradients (Pichon et al. 2011; Danovich et al. 2015). There it loses part of its angular momentum and flows to the DM halo.

At high redshift it is possible to see that inside the filaments the gravitational torque is \sim one tenth of the pressure torque. The picture changes when we look at the bottom panels, there the shocked filaments have a ratio $\tau_G/\tau_P \lesssim 10^{-2}$.

It is possible to find regions with a ratio $\tau_G/\tau_P > 10^{-2}$ around gas over-densities and near the main central halo. All the gas over-densities, in general associated to DM haloes at these scales, have a higher gravitational to pressure torque ratio. In particular at $z = 6$ we can see that the central galactic region for the NoSne simulation is dominated by the gravitational torque and for the Sne run the central region reaches a ratio $\tau_G/\tau_P \sim 1$ with a ratio gradient not as steep as in the NoSne. Such a behavior confirm the radial

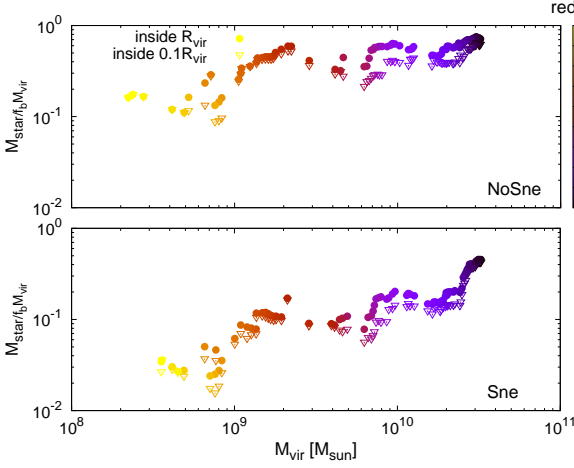


Figure 7. Halo mass - star mass (normalized by the halo baryonic content assuming that it has exactly the universal baryonic fraction f_b) relation as a function of redshift in different colors for our NoSne run at the top panel and our Sne run at the bottom panel. The filled circles mark the mass in stars inside the virial radius and the empty triangles mark the mass in stars inside one tenth of the virial radius. The small difference between the enclosed star mass at different radius shows that most of the stars are inside the central sphere of radius one tenth of the virial radius.

profile results of figure 14 and the α parameters of figure 12. At the edge of the galactic disc the pressure torque associated to the in-falling shocked material tends to dominate AM variations whereas at the central region the gravitational potential gradient is the main source of torque in the NoSne simulation. In the Sne run the energy injection spread out the high density material and there is a more flat potential at the center of the galaxy implying a non clear gravity domination there. Instead of that through the system evolution there is a mixed contribution between the pressure and gravity to the MT process, as we already have seen from the torques acting on the disc.

Having clear that the source of pressure gradients are the shocks associated to both the filamentary incoming material from the cosmic web and the SNe explosions it is interesting to elucidate the origin of the gravitational torque acting mainly on the central region of the galactic disc, because it works as a source of mass fueling the BH. In order to do that it is useful to study the density distribution on the disc. In particular, it is worth to compute the Fourier modes associated to the gas mass surface density:

$$c_m = \frac{1}{2\pi} \int_{-\pi}^{\pi} d\theta \int_0^{\infty} dr e^{im\theta} r \Sigma(r, \theta) \quad (37)$$

Figure 16 shows the square of each Fourier mode (from $m = 1$ to $m = 15$) normalized by $|c_0|^2$ for five different redshifts for both runs: NoSne in the top panel and Sne in the bottom panel. It is clear from the figure that the $m = 1$ mode has the higher power of the spectrum for all the shown redshifts. Despite of that, it is also possible to see that the difference in power between the first and the second mode is not too much for all the redshifts, i.e. $|c_2|^2/|c_1|^2 \gtrsim 0.5$. In this sense it is not possible to say that the first mode is the only contribution to the surface density spectrum because

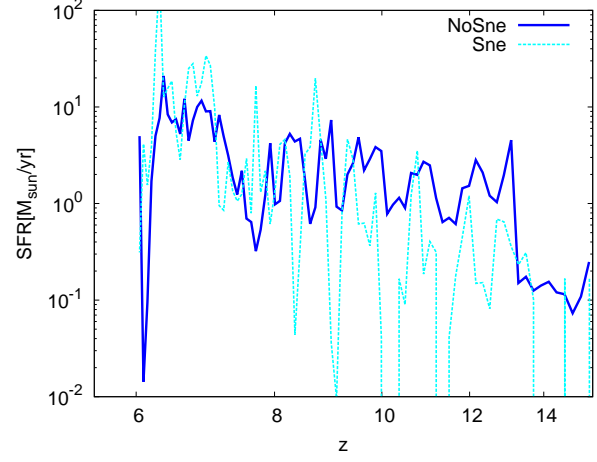


Figure 8. SFR as a function of redshift for the NoSne run in solid blue line and for the Sne run in dashed cyan line. It is worth to notice that at above redshift $z \approx 10$ the NoSne simulation presents a higher SFR compared with the Sne simulations. The NoSne experiment can form stars continuously without feedback. Below this redshift the dashed cyan peaks start to dominate the evolution showing that the Sne run is more efficient forming stars at some stages. In this case the SNe feedback can delay the star formation at high redshift due to the energy injection, but once the environment has been enriched by metals the gas can reach lower temperatures and higher densities enhancing the SFR producing the peaks associated to SF bursts.

the second mode is also important. Furthermore, it is worth to notice that the powers with $m > 2$ are also there and they have values $\gtrsim 10^{-2}$ below $m \approx 6$. It is interesting to compare our result with the one shown in Krumholz et al. (2007) where they found that the source of the torques on a proto-stellar disc is associated to the domination of the $m = 1$ mode due to the SLING instability (Adams et al. 1989; Shu et al. 1990). In their case the first power is at least one order of magnitude higher than the $m = 2$ mode with an increasing domination of $m = 1$ in time. They argue that the $m = 1$ spiral mode produce global torques which are able to efficiently transport AM. In our case, the global perturbation will be associated to a more complex disc structure. The reason for this difference will be clear after to look at the surface gas density projections.

Figure 17 reflects the fact that the power spectrum of the gas surface density shows powers for different modes m . There we can see a complex spiral-clumpy structure defining the galactic disc. Such a density field features create an inhomogeneous gravitational potential field which will exert torques on it surrounding media. In particular, the clumps formed on the disc by gravitational instabilities interact between them migrating to the central galactic region in short times of order as short as \sim few t_{orb} as can be deduced from the non rare short radial times of figure 13: the VDI works on these high redshift clumpy galactic discs (Bournaud et al. 2007).

It is worth to notice that due to the SNe energy injection in the Sne run the disc takes a longer time to appear compared with the NoSne experiment. Whereas the NoSne simulation develop a disc progressively in time disturbed no more than mergers the Sne run shows a disturbed clumpy

environment characteristic of turbulent gas. In particular the SNe run does not develop an spiral structure till $z \lesssim 9$. Before that the SNe explosions disrupt the galaxy with a strong effect on the central BH accretion rate as we will see in the next sub section. Furthermore, due to the metal release in the SNe run the gas can cool more efficiently than in the NoSne simulation. Such an important difference allows the gas to form more self gravitating over-densities and produce the clumpy galaxies shown at redshift $z \lesssim 8$ in the right column of figure 17.

3.4.4 Mass accretion and BH growth

High redshift galaxies are far from isolated systems and as has been shown above instead of that they are very dynamic in the sense that they are being built up in environments disturbed by filamentary accretion from the cosmic web, mergers and SNe explosions which affect the transport of AM. In the context of BH evolution at high redshift it is relevant to study and quantify the mass accretion rate on the galactic disc due to the processes described in the previous sub section, and more relevant yet is to quantify the mass accretion rate onto the central BH and related its mass accretion with the large scale structure filamentary inflows.

Figure 18 shows the radial gas mass accretion rate on the disc as a function of radius inside $0.1R_{vir}$ at different redshifts for our NoSne run in the top panel and for our SNe run in the bottom panel:

$$\frac{dM_g}{dt} = -2\pi r \Sigma_g v_r. \quad (38)$$

The figure shows intermittent lines due to the non-stationary and turbulent behavior of the gas. Such a features are another proof of the highly dynamic environment where the first galactic discs are formed: accretion, mergers, SNe explosions and clump-clump interactions are able to violently perturb the gas. The mass accretion rate fluctuates roughly between $\sim 10^{-2}$ and $\sim 10^2 [M_\odot/\text{yr}]$ in the range of radius shown in the figure. As mentioned above such a huge dispersion reflects the fluctuating condition on the galactic disc environment at high z , where due to its continue gas injection through filamentary accretion are far from a secular evolution as we can see in the low redshift galaxies.

In the SNe case it is possible to see that there is a clear increasing trend on the mass accretion rate at redshift $z = 7$. Such a feature is related with a number of simultaneous minor mergers bringing a large amount of material to the central halo region. At this time the galaxy is accreting a number of over-densities/in-falling gas (see redshift 7 of figure 17, in the NoSne case the main galaxy is being crossed by smaller galaxies whereas in the SNe case in is accreting a number of clumps) which are able to enhance the mass accretion rate ~ 2 order of magnitude compared with the previous and next sampled redshifts. It is worth to notice that after this enhanced on the mass accretion rate on the disc appears a clear drop on the BH mass accretion rate of figure 20 as we will discuss below.

When we compare the accretion rates on the galactic disc for our two experiments we can see that the NoSne run shows higher accretion rates. In this case the SNe outflows do not spread the gas out and the filamentary cold flows can reach the DM halo central region more easily.

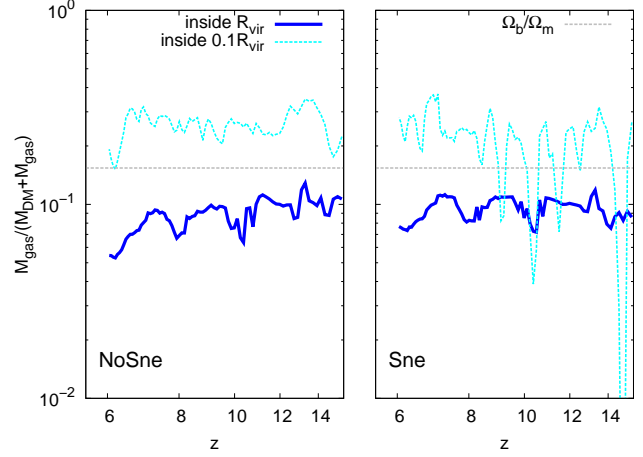


Figure 9. Gas mass fraction as a function of redshift for the NoSne run at the left panel and the SNe run at the right panel. Gas fraction inside the virial radius in solid blue line and gas fraction inside $0.1R_{vir}$ in dotted cyan line. The dashed gray line marks the universal baryonic mass fraction. Both systems show a high gas fraction inside the last tenth of the virial radius. The SNe run presents clear evidence of depletion due to SNe explosions. We have not included the mass of stars here which correspond to a negligible part $\lesssim 10^{-1}$ of the baryonic content.

The points near the y -axis mark the BH accretion rate. The BH accretion rate reaches values of order $\sim 10^1 [M_\odot/\text{yr}]$ at the end of the simulation for the NoSne and $\sim 10^0 [M_\odot/\text{yr}]$ at $z = 6$ for the SNe case. Such a ~ 1 order of magnitude difference between both runs clearly shows that the SNe explosions have an important impact on the mass accretion rate on the high redshift galaxies. It is interesting to note that such high values are not different compared with the ones observed on the disc inside the $0.1R_{vir}$. This feature shows that the mass is transported efficiently by the combined effect of pressure gradients and gravitational torques/VDI on the galactic disc at high redshift.

Because our galaxies are evolving inside a knot of the cosmic web it is natural to have non radial mass accretion on the disc. Figure 19 shows the \hat{z} to \hat{r} accretion rate ratio on the disc at the top for the NoSne run to the left and the SNe run to the right as a function of radius for different redshifts. The gray dashed line marks $|dM_{g,z}/dt|/|dM_{g,r}/dt| = 1$. The bottom panels shows the mass accretion rate on the disc in the \hat{z} direction, i.e. the mass accreted on directions parallel (and anti-parallel) to the gas AM vector. From the top panel it is clear that the \hat{r} direction dominates the mass accretion rate on the galactic disc. Despite of that there are radii and times where the \hat{z} direction dominates. Such high vertical accretion rates are associated to clumpy gas accreted perpendicular to the disc plane and they are mainly related with mergers of DM haloes.

The top plots of figure 20 shows the mass accretion rate onto the BH as a function of redshift in blue solid line for the NoSne simulation at the left panel and for the SNe simulation at the right panel. The dashed cyan line marks the Eddington accretion rate. Both panels show a clear difference between the accretion mode of the sinks through the system evolution. On one hand, the NoSne BH accretes al-

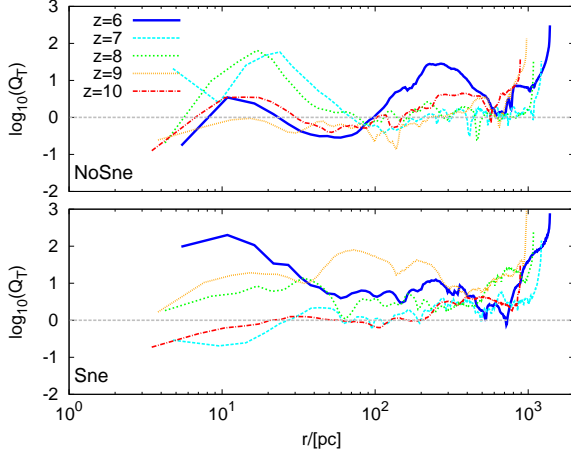


Figure 10. Toomre parameter as a function of radius for the NoSne run in the top panel and for the Sne run in the bottom panel at different redshifts: 6 in solid blue line, 7 in dashed cyan line, 8 in short dashed, 9 in orange dotted line and 10 in dotted-dashed red line. The Sne run shows higher values compared with the NoSne run. Such a difference has a direct relation with the SNe heating. The SNe explosions tends to stabilize the system under gravitational instabilities, increasing its Toomre parameter.

most at the Eddington limit until $z \sim 8$. At this redshift the galaxy suffers a number of mergers and the central part of the system loses a lot of gas leaving the BH with almost no material around to be consumed. After this event the accretion rate fluctuates till the end of the simulation. On the other hand, the Sne run shows a BH accretion with a lot of fluctuations until the end of the experiment. Such an intermittent evolution is due to SNe explosions mainly which are able to expel the gas out of the BH influence radius. This experiment shows a similar feature at $z \lesssim 8$ as in the NoSne run. In this case the mergers also perturb the mass accretion rate producing a clear drop on the mass consumption. It is interesting to relate this event with the enhanced radial mass accretion on the disc at $z = 7$ of bottom panel of figure 18. The accreted matter due to these mergers increase the radial MT at values $\sim 10^2 [M_\odot/\text{yr}]$, not so different compared with the NoSne run. Despite of this mass accretion rate increment the BH accreted mass also shows oscillations. The $\gtrsim 1$ order of magnitude difference in the mass accretion between our experiments shows that the SNe has a clear effect on the disc MT but despite of that the central massive object is able to grow considerably as we will show in the next lines.

As a complementary analysis, in the bottom panel of the same figure we shows the mass accretion rate ratio $f_{\text{EDD}} \equiv \dot{M}_{\text{BH}}/\dot{M}_{\text{EDD}}$ for both simulations. The NoSne run has an average fraction of $\langle f_{\text{EDD}} \rangle \approx 0.75$ and the Sne run $\langle f_{\text{EDD}} \rangle \approx 0.5$ through the BH evolution, which correspond to a $\sim 0.6 \text{ Gyr}$. If we average below $z = 8$ till the end of the simulation, i.e. the last $\sim 0.3 \text{ Gyr}$ we found that the NoSne ratio decreases to $\langle f_{\text{EDD}} \rangle \approx 0.5$ and the Sne ratio increases to $\langle f_{\text{EDD}} \rangle \approx 0.65$.

Figure 21 shows the BH mass evolution as a function of redshift for the NoSne run in solid blue line and for the Sne run in dashed cyan line. In this figure it is possible to see the effect of the different behavior in the accretion rate, as shown

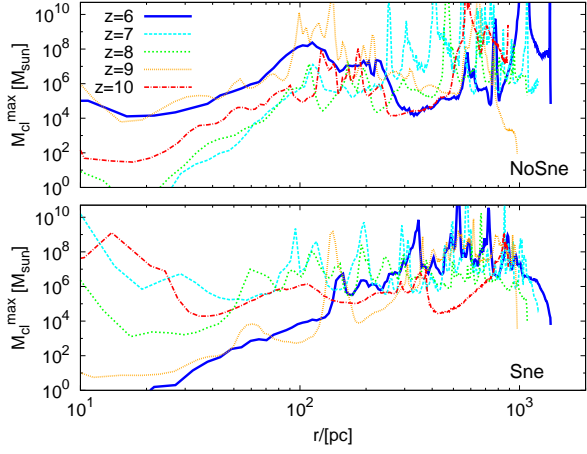


Figure 11. The maximum unstable mass in rotating disc as a function of radius for the NoSne run at the top panel and for the Sne run at the bottom panel for different redshifts: $z = 6$ in solid blue line, $z = 7$ in dashed cyan line, $z = 8$ in short-dashed green line, $z = 9$ in dotted orange line and $z = 10$ in dot-dashed red line. At scales of few $\sim 100 \text{ pc}$ the maximum mass is of the order $\sim (10^4 - 10^8) M_\odot$, showing a huge scatter associated to the clumpy gas disc.

in figure 20. Whereas the NoSne sink has an approximately exponential evolution ending with a mass $M_{\text{BH}} \sim 10^9 M_\odot$ the sink of our Sne run grows much more slower ending with a mass $\sim 6 \times 10^7 M_\odot$. For the NoSne run, the most prominent deviation from the approximately exponential growth appears below $z = 8$ in the NoSne simulation due the simultaneous minor mergers which are able to drop the mass accretion rate in both experiments.

3.5 Mass transport on larger scales

Because in a cosmological context at high redshift we can not study the small-galactic scale phenomena without take into account the effects of the large scale structure here we study the behavior of the mass accretion rate above the $\sim \text{kpc}$ scales, i.e. beyond the galactic disc edge.

Figure 22 shows the mass accretion rate till the $\sim 3R_{\text{vir}}$. The mass accretion has been computed taking into account all the mass crossing a spherical shell at a given radius:

$$\frac{dM_g}{dt} = -4\pi r^2 \rho v_r. \quad (39)$$

The left column of figure 22 shows the total mass accretion rate for the NoSne simulation at the top panel and for the Sne simulation at the bottom panel. At the right column we have plotted the mass accretion rate associated to gas densities below the threshold density for gravitational collapse in the spherical collapse model: $\rho_{\text{coll}} = 18\pi^2 \Omega_b \rho_c / \Omega_m \approx 200 \Omega_b \rho_c / \Omega_m$, with ρ_c the critical density of the Universe. The vertical lines mark the DM virial radius at each redshift. The right column of the figure can be interpreted as smooth accretion associated non collapsed objects. The NoSne top-right panel shows a smooth decreasing behavior almost independent of redshift. The smooth mass accretion rate presents roughly constant values above the virial radius, with accretion rates of the order $\sim 10^2 M_\odot/\text{yr}$.

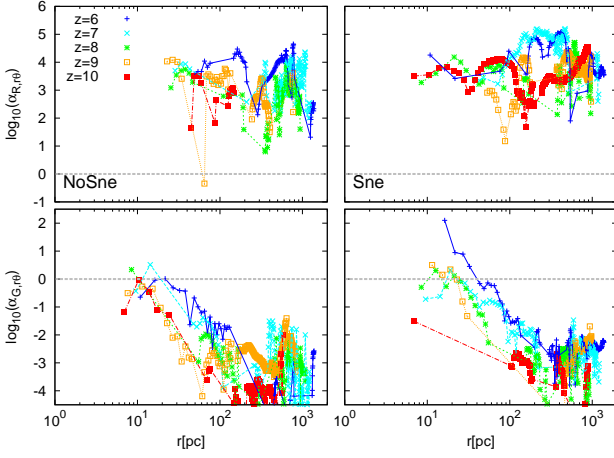


Figure 12. The $\alpha_{r\theta}$ parameters on the disc as a function of radius for different redshifts: $z = 6$ in blue cruxes, $z = 7$ in cyan x's, $z = 8$ in green asterisks, $z = 9$ in orange squares and $z = 10$ in red filled squares. The gray dashed line marks the $\alpha = 1$ position. The left column show the NoSne results and the right column the Sne results. In the top rows appear the Reynolds α and in the bottom row the gravitational α . It is clear that the bulk inertial motion dominates in the rate of momentum flux and the pressure dominates over the gravity most of the time. The gravitational α parameter has a decreasing trend with radius showing that the gravitational stress tends to be more important than pressure at the center of the system.

On the other hand, the bottom-right Sne run panel has a more irregular decreasing behavior with a notorious dependence in redshift due to SNe explosions, i.e. due to the dispersion of matter after the energy injection. In particular for redshifts lower than 10 it is possible to see that the smooth accretion is practically erased at small radii compared with the NoSne run, a clear signal of low density gas evaporation. In other words, due to SNe explosions only the dense gas is able to flow into the $\lesssim 1$ kpc region of the galaxy.

It is interesting to note that for both runs the smooth accretion goes from $\sim 10^2 M_\odot/\text{yr}$ at the outer region of the DM halo to $\sim 1 M_\odot/\text{yr}$ at the border of the inner ~ 1 kpc region. On the other hand, the total mass accretion can reach peaks of few $\sim 10^5 M_\odot/\text{yr}$ associated to gas clumps falling into the DM halo. The total large scale mass accretion rate for both runs is $\sim \text{few } 10^3 M_\odot/\text{yr}$.

It is worth to notice that above the virial radius the smooth accretion is the floor of the total mass accretion rate. At smaller radii the total mass accretion floor tends to be higher than the smooth accretion. It can be understood if we note that at smaller radii the material tends to be at densities above the collapsed density, then most of the accreted gas is in a non-smooth accretion state. All the mass accretion rate peaks are associated to over densities due to both gas clumps mainly inside DM haloes (see figure 1).

Figure 23 shows the total mass accretion of the system from $\sim \text{few pc}$ to $\sim \text{few } 10$ of kpc for the NoSne run in the top panel and for the Sne run in the bottom panel. It is very interesting to note that the mass accretion rate tends to decrease until one tenth of the virial radius. In other words, not all the material at few virial radius (with a floor on the accretion rate of the order $\dot{M} \sim 10^2 M_\odot/\text{yr}$ and an average

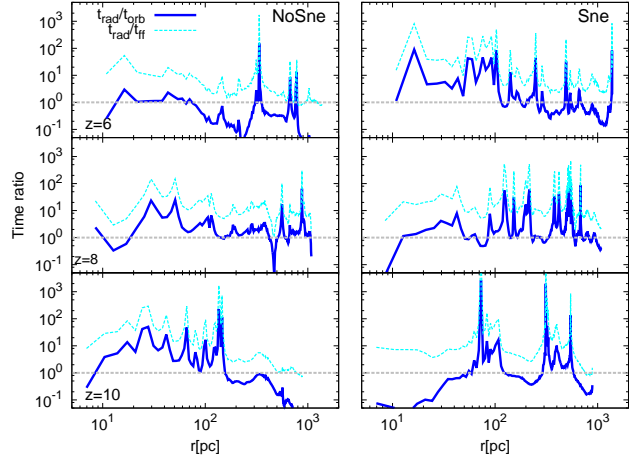


Figure 13. Radial profiles of the $t_{\text{rad}}/t_{\text{orb}}$ ratio in solid blue line and $t_{\text{rad}}/t_{\text{ff}}$ ratio in dashed cyan line for three different redshifts in different rows and for the NoSne run in the left column and the Sne run in the right column. The $t_{\text{rad}}/t_{\text{orb}}$ ratio shows that the system presents at different times regions with $t_{\text{rad}} \sim t_{\text{orb}}$, a clear proof of its highly dynamical condition. On the other hand the ratio $t_{\text{rad}}/t_{\text{ff}}$ is of order unity at the outer disc region as a consequence of the free falling. At the inner regions of the disc this ratio increases due to the effect of gas pressure which does not allow the gas to continue the free falling.

of $\sim 10^3 M_\odot/\text{yr}$) is ending its travel on the galactic disc region. Such a phenomenon is easily explained if we note that the filaments reach the DM halo with a given impact parameter, i.e. they do not fall exactly on the galactic center. Such an effect does not allow to a fraction of gas to reach the central region before some crossing times if they can loose part of their AM. In fact, at the border of the galaxy the accretion rate has decreased ~ 2 order of magnitude until $\dot{M} \sim 10 M_\odot/\text{yr}$ in both simulations. Inside one tenth of the virial radius, i.e. on the galactic disc, the average slope of the data tends to be more flat with values fluctuating roughly from $\sim 10^{-2} M_\odot/\text{yr}$ to $\sim 10^2 M_\odot/\text{yr}$: a proof of the highly dynamical and far from stationary nature of the high redshift galactic discs.

From our results it is possible to compare the large scale accretion rate with the BH accretion rate at the end of the simulation. It is interesting to note that for the NoSne run the mass accretion on the BH is ~ 2 order of magnitude lower than the large scale accretion rate at $z = 6$ and for the Sne run it is ~ 3 order of magnitude lower. Because at large $\gtrsim R_{\text{vir}}$ scales both experiments show similar accretion rates of order $\dot{M} \sim 10^3 M_\odot/\text{yr}$ we can say that the SNe feedback affect the system evolution at scales $\lesssim R_{\text{vir}}$, i.e. inside the virial sphere. As a final remark, we see that in the Sne simulation the mass accretion rate on the galactic disc is a fraction of $\sim 10^{-3}$ the mass accretion rate at large scale $\gtrsim R_{\text{vir}}$ through the simulation. Such a number is similar to the proportionality factor between the BH mass and the galactic bulge mass (Marconi & Hunt 2003) which is connected with the $M_{\text{BH}} - \sigma$ scaling relation Ferrarese & Merritt (2000); McConell et al. (2011). In this sense we speculate with a potential relation between the ratio of the mass accretion rate at different radius and the BH mass - bulge

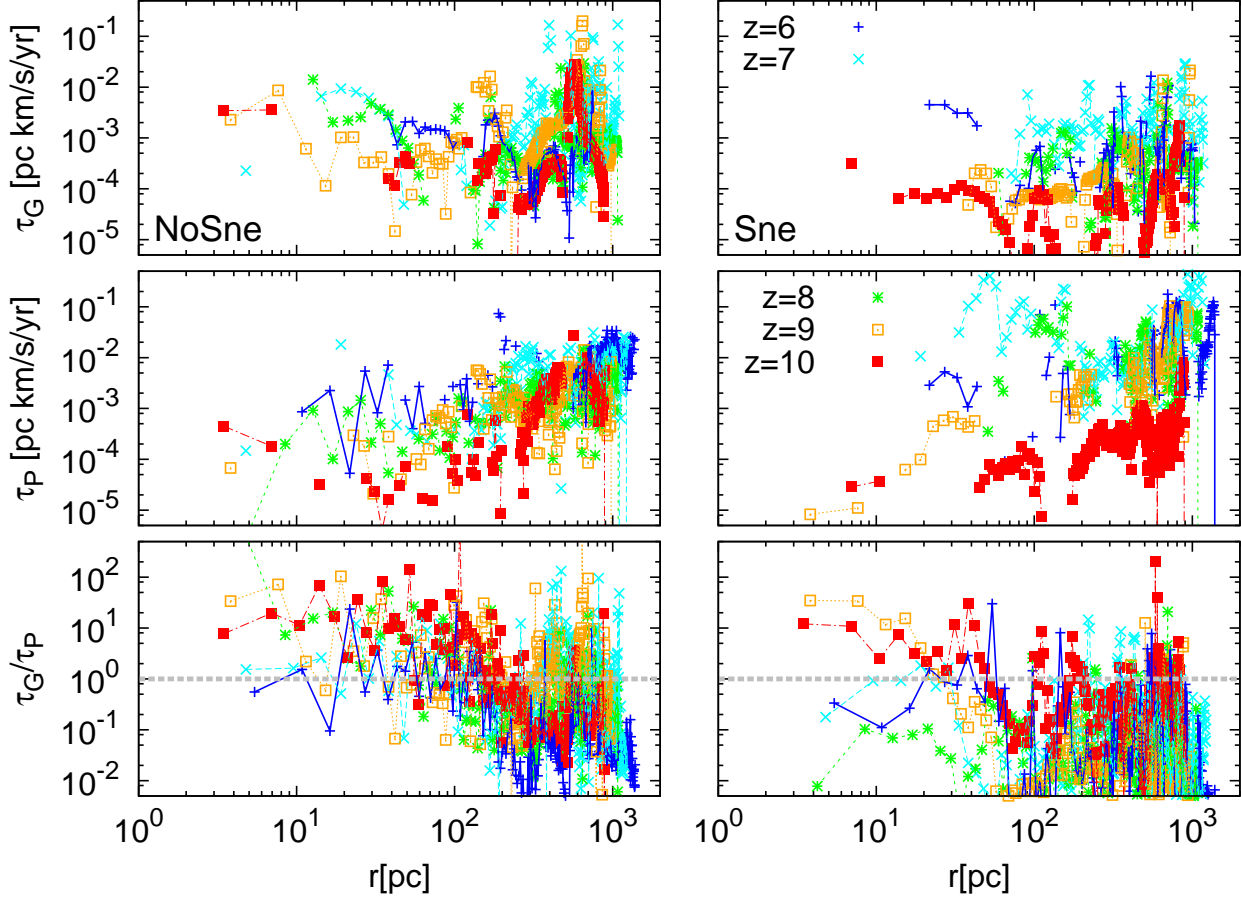


Figure 14. Top panels: Show the gravitational torque associated to inward MT for the NoSne run to the left and for the Sne run to the right at different redshifts: $z = 6$ in blue crosses, $z = 7$ in cyan x's, $z = 8$ in green asterisks, $z = 9$ in orange squares and $z = 10$ in red filled squares. For both runs there is no clear trend in radius. Central panels: Show the pressure torque associated to inward MT. Both runs show a roughly decreasing trend in radius with higher torques at larger radii. The Sne run shows a much larger data dispersion due to SNe explosions. Bottom panels: Show the modulus of the gravitational to pressure torques ratio. The previous trend is reflected in this quantity with an roughly increasing trend implying that at small radius the gravity torques tend dominate the AM variations.

mass relation. Certainly such a hypothetical statement need further studies to be confirmed or ruled out.

3.6 Gas-stars-BH spin alignment

As a complementary analysis it is interesting to study the alignment between the spin of the different component of the system, namely DM, gas and stars. Figure 24 shows the alignment between the spin of the different components of the system: the angle between the gas spin and the BH spin appears in dashed green line, the angle between the gas spin and stars spin appears in solid blue line and the angle between the gas and DM spin is in dotted orange line. The misalignment angle between the gas spin \vec{l}_{Gas} and the component i of the system \vec{l}_i was computed as:

$$\theta_{Gas-i} = \frac{\vec{l}_{Gas} \cdot \vec{l}_i}{|\vec{l}_{Gas}| |\vec{l}_i|} \quad (40)$$

The rotational center to compute the gas, DM and stars spin was set as the sink position, \vec{r}_{sink} . This point coincides

with the gravitational potential minimum cell within ~ 50 pc around the sink particle.

We estimated the BH spin as

$$\vec{l}_{BH} = \sum \Delta m_{sink} (\vec{r}_{cell} - \vec{r}_{sink}) \times (\vec{v}_{cell} - \vec{v}_{sink}), \quad (41)$$

with \vec{r}_{cell} the center of the cell where the sink is located at the maximum level of refinement, \vec{v}_{cell} is the gas velocity inside the cell, \vec{v}_{sink} is the sink velocity and Δm_{sink} is the accreted mass at each fine time step. Here we strength that the sink position is not the same as the center of the cell where the sink is located, then the radial vector difference is not null. Despite of the expression above is not the correct BH spin acquisition formula it will give as an idea about the spin of the material falling into the BH.

From the figure we can see that the gas and the DM spins are far from aligned. The misalignment angle between them fluctuates from a parallel alignment ($\theta_{Gas-DM} \approx 10^\circ$) to an almost anti-parallel configuration ($\theta_{Gas-DM} \approx 160^\circ$). Such a non-correlation between the spin of these two components has been studied before in, e.g. Prieto et al. (2015).

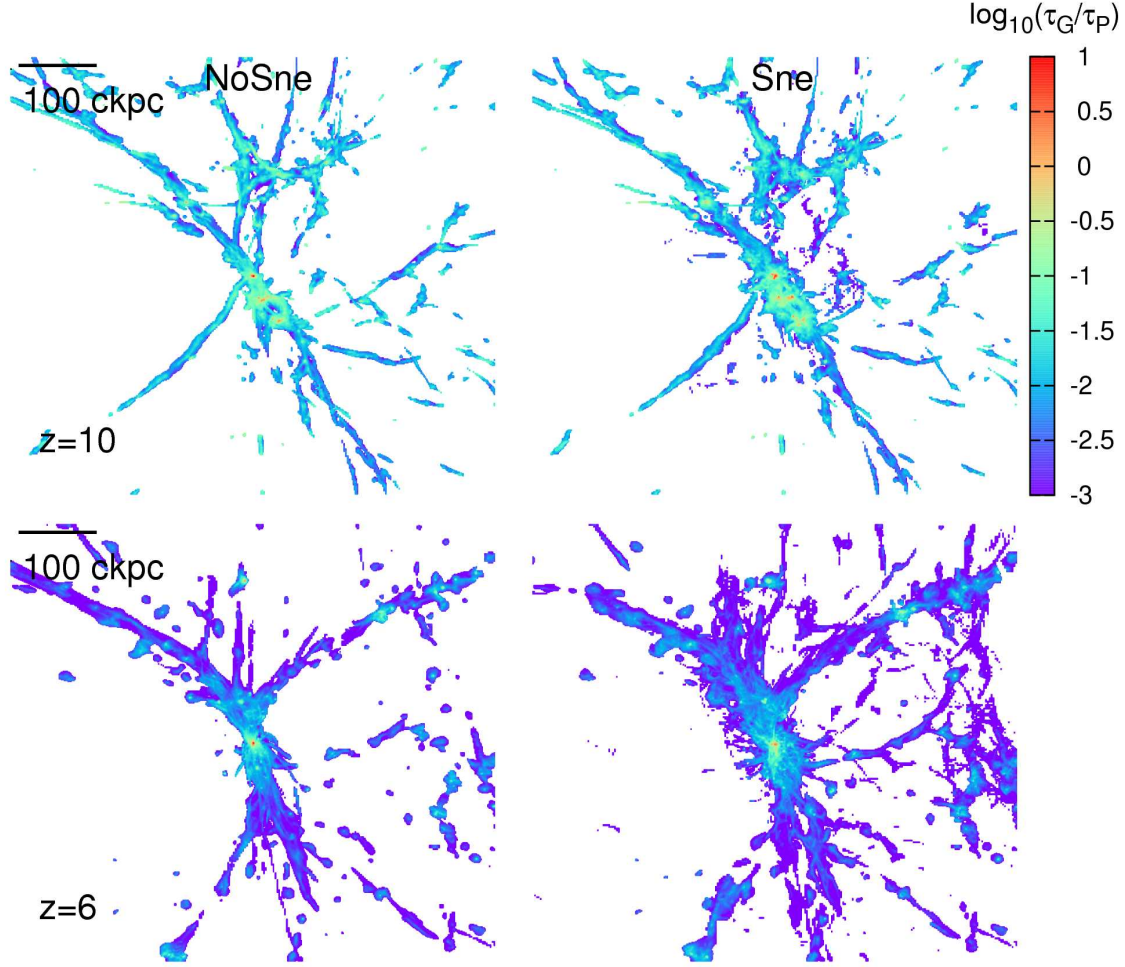


Figure 15. Modulus of the mass weighted gravitational to pressure torque ratio at $z = 10$ in the top row and at $z = 6$ in the bottom row. The left column shows the NoSne run and the right column the Sne run. It is interesting that the pressure torque dominates over the gravitational one in most of the mapped filamentary dense regions. The gravitational torque increases its influence at the central region of filaments and around gas over-densities. Such a fact confirm our previous finding based on the torques ratio radial profiles: gravitational torque increases its influence at the central galactic region.

In their work the authors noticed that after the turn around the gas can decouple from the DM due to its collisional nature: whereas the DM can feel only the gravity the gas can also feel the gas pressure. In their work the pressure gradient working on the gas associated to a $\sim 10^9 M_\odot$ DM halo at redshift $z = 9$ is responsible of an extra torque on the baryonic component and its spin deviates from the DM spin orientation. As we already shown in figure 14 the pressure gradients are not negligible inside the virial radius of the halo. Such torques are able to change the orientation of the gas AM and then create a misalignment between gas and DM spin vectors.

The alignment between gas and stars in solid blue line has a different behavior in our runs. For the NoSne case it is possible to see that at high redshift, between $z \approx 15$ and $z \approx 13$, the stars and the gas had a very different spin orientation. This is because at this stage the galaxy is starting to be built by non spherical accretion and mergers, conditions which does not ensure an aligned configuration. After $z \approx 13$ the gas and stars reach a similar spin orientation with a misalignment angle fluctuating between $\theta_{Gas-Stars} \approx 40^\circ - 20^\circ$.

There the proto-galaxy can not be perturbed easily by minor mergers and acquire a defined spiral shape allowing the gas-star alignment. Such an alignment is perturbed at redshift $z \approx 10$. At this redshift the main DM halo suffers a number of minor merger which can explain the spin angle perturbation. After that the gas and stars again reach an aligned configuration until the end of the simulation.

The Sne run shows a much more perturbed gas-stars spin evolution. In this case, due to the SNe explosions the gas is continuously perturbed due to the energy injection. The strong shocks associated to this phenomenon are able to decouple the gas from the stars spin. The gas and stars can not be aligned before $z \lesssim 8.5$ where the mass of the disc is high enough to do not be significantly disturbed by the local SNe energy injection (see figure 17). In this case the DM again does not follow the gas and both components are misaligned most of the time.

The dashed green line shows the gas and BH spin angle alignment. In both simulations it is possible to see that the misalignment angle fluctuates a lot through the system evolution. Despite of that in both cases the angle decreases

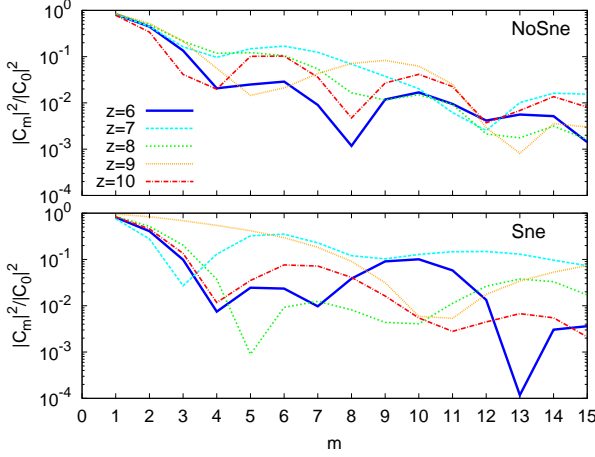


Figure 16. The Fourier modes associated to the mass surface density on the disc. The power spectrum is plotted for the NoSne run in the top panel and for the Sne run in the bottom panel. Each curve marks a different redshift: $z = 6$ in solid blue line, $z = 7$ in dashed cyan line, $z = 8$ in short dashed green line, $z = 9$ in dotted orange line and $z = 10$ in dot-dashed red line. Despite of the $m = 1$ mode has the higher power, the mode $m = 2$ is also important being a fraction $\gtrsim 0.5$ of the $|c_1|^2$ at all redshifts. Furthermore, all the other $m > 3$ modes have a contribution of roughly similar order between them. In other words, the disc have developed a complex azimuthal structure allowing gravitational torques.

at the end of the simulation showing an alignment between the gas and the BH spin at $z \lesssim 8$. A qualitatively similar behavior can be seen in Dubois et al. (2014). In general it has roughly a similar behavior compared with the gas-stars spin orientation. It implies that at the end of the simulation the gas, stars and the BH angular momentum are aligned with a $\theta \lesssim 40^\circ$ but due to its non collisional nature the DM AM has a misalignment of $\theta_{Gas-DM} \approx 90^\circ$ at the end of the experiments.

4 DISCUSSION AND CONCLUSIONS

By using cosmological hydrodynamic zoom-in simulations we have studied the MT process from \sim few 10 kpc to \sim few pc scales on a DM halo of $M \approx 3 \times 10^{10} M_\odot$ at redshift $z = 6$. We have studied the evolution of the system with (Sne run) and without (NoSne run) SNe feedback.

Following to Gammie (2001) we have computed the α parameters associated to both the Reynolds and the gravitational stresses. In other words, we have computed both the Reynolds and the gravitational rate of momentum fluxes on the disc normalized by the gas pressure. Gammie (2001) showed that the α parameters associated to radial mass transport are of order $\alpha \sim 10^{-2}$, reasonable values for a subsonic stationary accretion disc. In our case the α parameters had values well above unity, it means that both the Reynolds and the gravitational rate of momentum flux (in some cases) have values higher than the gas pressure. Such a high values are characteristic of a turbulent super-sonic environment associated to dynamical systems. The non sta-

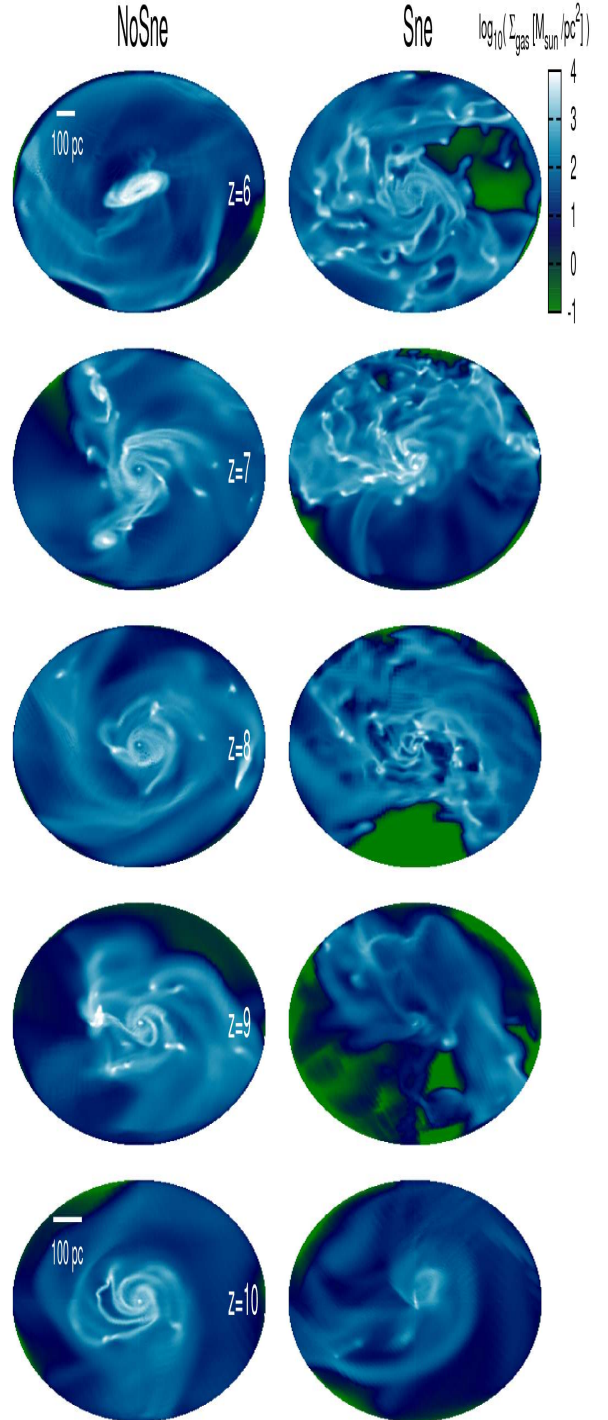


Figure 17. Gas surface density projections for the NoSne run to the left and for the Sne run to the right at different redshifts from $z = 6$ to $z = 10$ from top to bottom. The evolution of the density maps show that the galaxy develops a complex spiral clumpy structure supporting the existence of high m powers in the Fourier analysis of figure 16. Due to SNe explosion the spiral shape of the object appears only at $z \lesssim 8$ in the Sne run. Below this redshift the galaxy is successively destroyed by SNe and re-built by gravity.

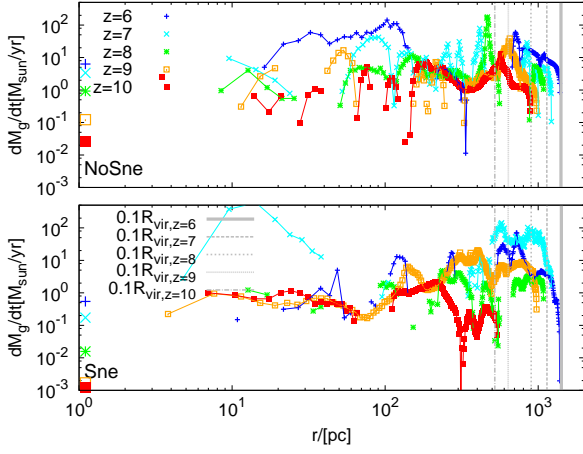


Figure 18. Mass accretion rate radial profiles for the NoSne simulation in the top panel and the Sne simulation in the bottom panel at different redshifts: $z = 6$ in blue crosses, $z = 7$ in cyan x's, $z = 8$ in green asterisks, $z = 9$ in orange squares and $z = 10$ in red filled squares. The vertical lines mark the $0.1R_{vir}$ at each redshift. The big points close to the y-axis mark the BH accretion rate at the corresponding redshift. In both simulations the accretion rate has huge fluctuations between $\sim 10^{-2}$ and $\sim 10^2 [M_\odot/\text{yr}]$, another proof of the highly dynamic nature of the system. The Sne run shows a mass accretion rate about ~ 1 order of magnitude lower than the NoSne simulation on the disc, i.e. $\sim 1 [M_\odot/\text{yr}]$.

tionary gas behavior is confirmed also by the highly fluctuating values of α at all redshift.

We found that the Reynolds stress dominates over the gravitational one through the simulations. Here it is worth to note that the Reynolds stress tensor is a measurement of the flowing material on the galactic disc. In these systems the gas falls from large scales channelized by filaments almost freely onto the DM halo central region getting supersonic velocities with a huge radial component. Under such a conditions the rate of momentum flux associated to this term normalized by the gas pressure, i.e. divided by $\sim \rho c_s^2$, will be much higher than 1. We strength that the Reynolds stress is not a source of mass transport but it is a measurement of the local rate of momentum transport triggered by other processes, namely pressure gradients, gravitational forces, magnetic fields or viscosity. In this sense, its high value is just telling us that through the galaxy evolution do exist processes capable to transport mass from large scales to small scales very efficiently. In fact, in our systems the gravity trigger the mass flows through the DM filamentary structure around the central halo. The Reynolds term tends to be higher for the Sne run where the energy injection allows the gas to reach higher velocities.

The gravitational α parameter tends to be lower than 1 at high redshift, $z \gtrsim 8$. Its values reach a peak $\alpha_G \lesssim 10$ at lower redshifts and near the center of the galaxy, $r \lesssim 100$ pc. It means that the gravitational potential gradients at the galactic central regions are able to transport mass more efficiently at low z than at high z allowing a more efficient BH fueling. The gravitational α parameter shows a decreasing shape with the galactic radius until $r \lesssim$ few 100 pc. It tends to be lower at larger radii. Such a behavior is present in

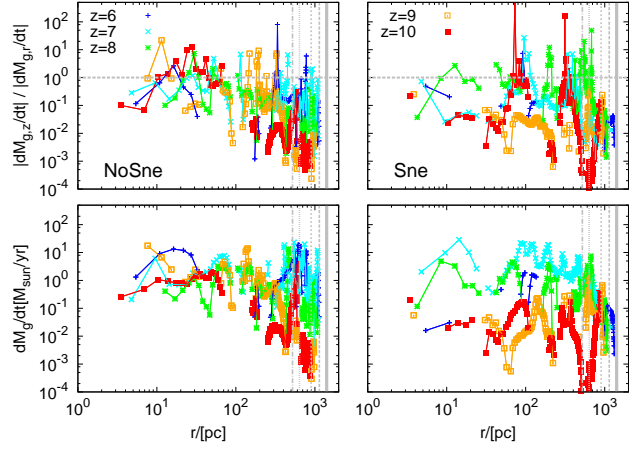


Figure 19. Top panels: The ratio between the \hat{z} and the \hat{r} mass accretion rate for the NoSne simulation to the left and the Sne simulation to the right for different redshifts: $z = 6$ in blue crosses, $z = 7$ in cyan x's, $z = 8$ in green asterisks, $z = 9$ in orange squares and $z = 10$ in red filled squares. The vertical lines mark the $0.1R_{vir}$ at each redshift. The \hat{r} accretion dominates on the galactic disc, despite of that there are peaks of \hat{z} accretion mainly associated to mergers. Bottom panels: Same as figure 18 but for the \hat{z} accretion showing the NoSne simulation to the left and the Sne simulation to the right.

both runs. At higher radius it tends to be well below 1 and roughly constant until the border of the galaxy, ~ 1 kpc.

Comparing the orbital, radial and free-fall time of our systems we found that at the outer edge of the disc the gas tends to be in free-fall. It decreases its velocity once reaches the high density region associated to the galactic disc. There the gas pressure stop the free-falling travel from the cosmic web. Such a high radial velocity at the disc edge is partially kept at smaller radii where the baryonic matter can show radial times similar to orbital times, i.e. radial velocities similar to the orbital velocity. Despite of the outflows associated to SNe explosions we can see these high radial velocities in both runs showing that the SNe explosions are not enough strong to stop the accretion of dense material through DM filaments (Powell et al. 2011).

The torques associated to the gravitational potential gradient is not so different in both runs. The main difference in torques between these two experiments appears in the pressure torques. Whereas the NoSne run shows a roughly decreasing in radius behavior the Sne run has a much more spread range of values barely showing a decreasing trend with radius. The comparison between them, i.e. the ratio between the gravitational and pressure torque, shows that without SNe the gravity tends to dominate the AM transport on the galactic disc at radius $r \lesssim$ few 100 pc. Beyond this radius there is a mixed contribution on torques with regions dominated by gravity and others by pressure at different times. The Sne run also shows a mixed behavior at small radius $r \lesssim 100$ pc, with gravity dominating at high redshift and pressure at low redshifts. In this case at larger radius it is more clear the pressure domination. In other words, in the Sne run the AM transport tends to be dominated by pressure gradients at large radii. Despite of that

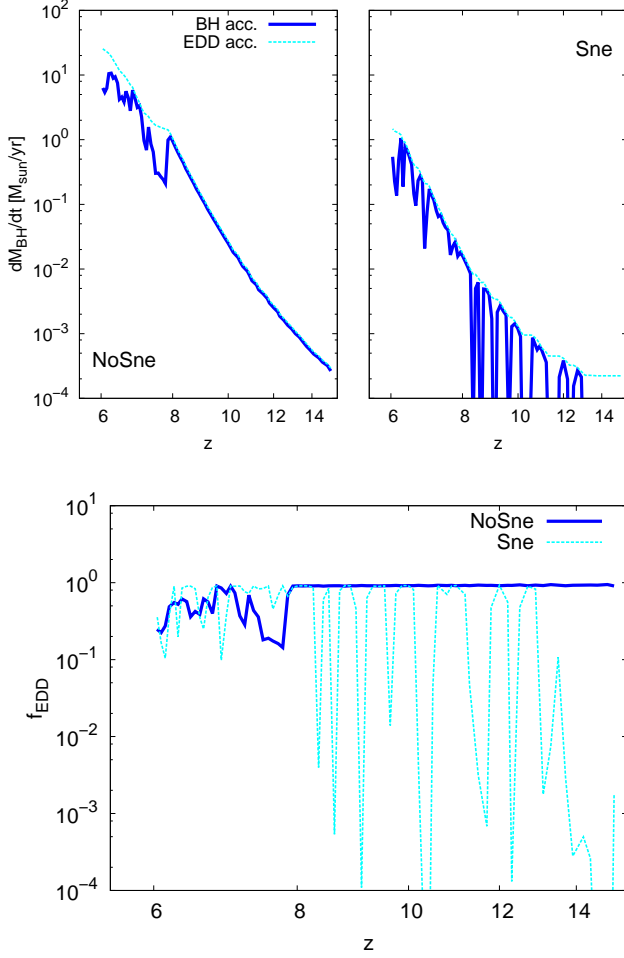


Figure 20. Top: The BH mass accretion rate as a function of redshift in solid blue line for the NoSne experiment to the left and the Sne experiment to the right. The cyan dashed line in both panels marks the Eddington accretion rate at the corresponding redshift. It is worth to notice that the BH accretion rate is Eddington limited most of the time with a big perturbation below $z = 8$ in the NoSne run associated to a gas rich DM halo merger. The Sne run shows a number of fluctuations associated to the SNe explosions through the galaxy evolution. Bottom: the BH mass accretion rate normalized by the Eddington accretion, f_{EDD} in solid blue line for the NoSne run and in cyan dashed line for the Sne run. It has an average value of $\langle f_{\text{EDD}} \rangle \approx 0.75$ in the NoSne case and $\langle f_{\text{EDD}} \rangle \approx 0.5$ in the Sne through the BH evolution.

it is also possible to observe gravity dominated regions at different redshift on the disc, in particular at the central $r \lesssim 100$ pc region fueling the BH. In fact, the SNe energy injection creates strong pressure gradients which are able to transport mass and AM on the disc, and at the same time the enhanced cooling due to metals create a gravitationally unstable density field. Such a conditions allow gas clumps formation and interaction. The over-densities can interact between them and with the galactic spiral arms also enhancing the gravitational torques on the disc (VDI), such a process is more relevant at the center of the galaxy.

When we look at the large scales related with the filamentary structure around the central DM halo it is possible to see that the pressure torques dominate over the gravita-

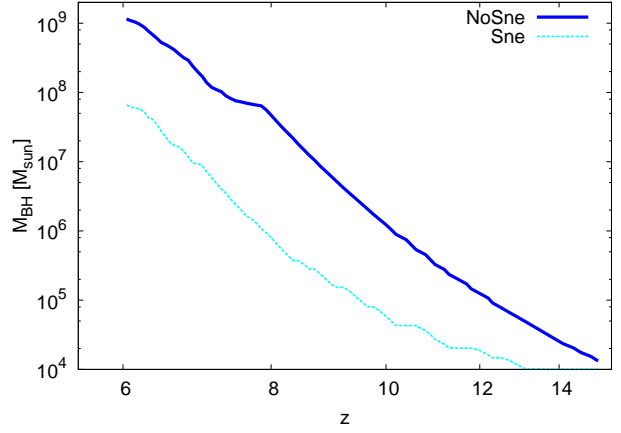


Figure 21. BH mass evolution for our NoSne simulation in solid blue line and for our Sne simulation in dashed cyan line. The NoSne sink particle reaches the $\sim 10^9 M_{\odot}$ at the end of the simulation. Such a high mass was reached because most of the time the BH were accreting to the Eddington limit. On the other hand, the Sne run sink reaches a final mass of $\sim 6 \times 10^7 M_{\odot}$ due to the constant accretion interruption due to the SNe energy injection and mergers.

tional torque in filaments. The central region of the filaments shows an enhanced gravitational contribution but it is not enough to be dominant. These results are consistent with the picture in which the material filling the voids falls onto the filamentary over-densities where it is channelized to the central DM halo region (Pichon et al. 2011; Danovich et al. 2015) by gravity. Once the gas reaches the filaments it feels the pressure gradient on the filaments edge and it loses part of its AM. Then the gravity works and transport the mass almost radially inside the cold filaments to the central region of the DM halo. Such a process allow the gas to reach the galactic edge almost at free-fall. There the gas pressure works reducing its initially high radial velocity but at the same time exerting torques allowing the MT. Through out this process the gravitational torques also work on the gas helping to the MT process on the disc.

A Fourier analysis of the gas surface density field for both runs shows that the density power spectrum have a lot of excited modes. Despite of the $m = 1$ and $m = 2$ modes dominate the power spectrum the other modes do exist and have roughly comparable values between them. Such a feature tell us that the gas surface density develop a complex structure through its evolution. The information given by the Fourier analysis is confirmed by visual inspection. The galactic discs develop spiral arms and gas clumps which interact between them by gravity. The gas clumps are formed from the cold and almost pristine gas flowing from the cosmic web onto central DM halo region. The high gas fraction (which can be as high as 30%) and cold environment is a perfect place to produce a clumpy galactic disc. The interaction between gas clumps, spiral arms and merged DM haloes exert gravitational torques which are capable to transport mass onto the galactic center in times comparable to the dynamical time of the system: it is the so-called VDI (Mandelker et al. 2014; Bournaud et al. 2007).

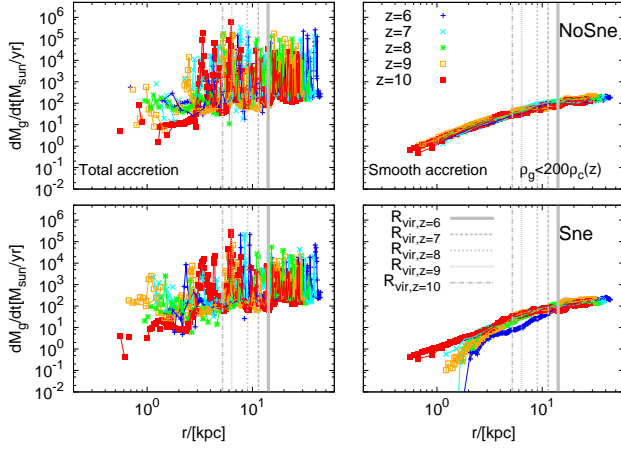


Figure 22. Left column: Same as figure 18 but for larger radii taking into account material till $\sim 3R_{vir}$ around the central halo. The top panel shows the NoSne case and the bottom panel the Sne case. Right column: Same as left column but for the smooth accretion, i.e. for gas with a density below the collapse density $\rho_{coll} \approx 200\Omega_b\rho_c/\Omega_m$. At large radii the total accretion has a floor similar to the smooth accretion with a lot of accretion rate peaks associated to collapsed dense gas clumps and DM haloes. At lower radii the gas tends to be above the collapsed density then the accretion associated to this component decreases and it is not similar to the total accretion floor. The SNe explosions have a clear effect on the smooth accretion. At \sim kpc scales the smooth accretion is erased due to the outflows.

Due to the process exposed above, i.e. large scale gravitational collapse inducing filamentary accretion onto the DM central region and both gravitational and pressure torques acting on the galaxy, the mass can flow through the galactic disc and reaches the galactic center. The radial mass accretion rate inside $\sim 0.1R_{vir}$ has huge fluctuation with values in the range $(10^{-2} - 10^2)M_\odot/yr$, a clear proof of a non-stationary and highly dynamic environment. Such a dynamic environment rises as the result of a large and almost radial gas flow entering the virial sphere, clump formation due to both the low temperature and the high gas density on the disc, the interaction and migration of these clumps on the disc and the merger events suffering by the host DM halo. In general the NoSne run shows a higher mass accretion rate with values of order $\sim 10M_\odot/yr$ whereas our Sne run shows a mass accretion rate of $\sim 1M_\odot/yr$ at the central region of the galaxy.

Certainly the position of the galaxy inside a knot of the cosmic web does not constrain the accretion process to the disc radial direction and then do exist a vertical mass accretion contribution. The \hat{z} component of the gas does not dominate the mass accretion rate but it has density peaks associated to gas over-densities reaching the disc on the vertical direction which exert torques on the gas enhancing the VDI.

The high mass accretion rate on the high gas fraction disc allows the central BH to grow at the Eddington limit most of the time for the NoSne run whereas in the Sne run it is clearly affected by the SNe explosions showing intermittent Eddington limited accretion rate. Despite of that it can increase its mass substantially through out the simulation.

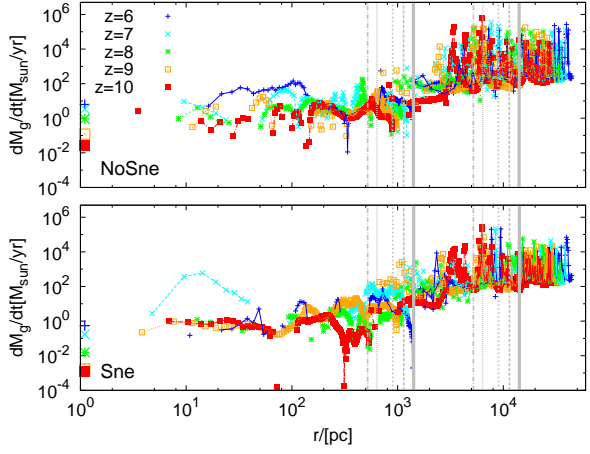


Figure 23. Same as figure 18 but for a larger range in radius showing the accretion rate from \sim few 10 kpc down to \sim few pc.

The violent events, namely mergers (which can also trigger mass accretion torquing the gas on the disc) and SNe explosions are not enough to stop the BH growth. The 10^4M_\odot BH seed can evolve until the $\sim 10^9M_\odot$ in our NoSne experiment and until $\sim 6 \times 10^7M_\odot$ in our Sne experiment at redshift $z = 6$. The factor ≈ 15 in difference shows that the SNe do affect the BH evolution but they are not able to stop it growth in these clumpy and high gas fraction systems.

When we look at the mass transport beyond the virial radius we found that the large scale $r \gtrsim R_{vir}$ mass accretion rate has a floor of the order $\sim 10^2M_\odot/yr$ with peaks associated to gas inside DM haloes of $\sim 10^5M_\odot/yr$ and an average of the order $\sim 10^3M_\odot/yr$ for both runs. Due to the non-spherically symmetric mass flows the mass accretion rate floor at $\sim 0.1R_{vir}$ is $\sim 1 - 10M_\odot/yr$, i.e. lower than the accretion at virial radius. In other words, material with a large impact parameter will not reach the virial sphere before some crossing times if it is able to loose part of its AM. Beside this effect, the SNe explosions will spread part of the gas out of the virial sphere decreasing the filamentary accretion efficiency.

At the end of the simulations the BH accretion rate is about $\sim 10^{-1}$ the accretion rate at the galactic edge and it is $\sim 10^{-3}$ the accretion rate beyond the virial radius for our Sne run. Furthermore, trough the simulation we could see that the mass accretion on the galactic disc is roughly $\sim 0.1\%$ of the cosmic accreted material. This number is translated to a galactic disc accretion efficiency of $\sim 10^{-3}$ when we compare it with the large scale baryonic mass accretion rate, which is a factor similar to the proportionally factor found in the M_{BH} scaling relation (Marconi & Hunt 2003).

The gas spin vector orientation fluctuates a lot with respect to the DM spin vector through the system evolution. The gas and DM start their evolution with spin vectors roughly aligned but once the pressure gradients increases due to virialization shocks (Prieto et al. 2015) and SNe explosions they decouple reaching an almost anti-parallel orientation at some stages. In both simulations the DM and gas finished their evolution with a misalignment of $\sim 100^\circ$. The gas and stars have a more coupled evolution. In this case they start with a given misalignment due to the chaotic

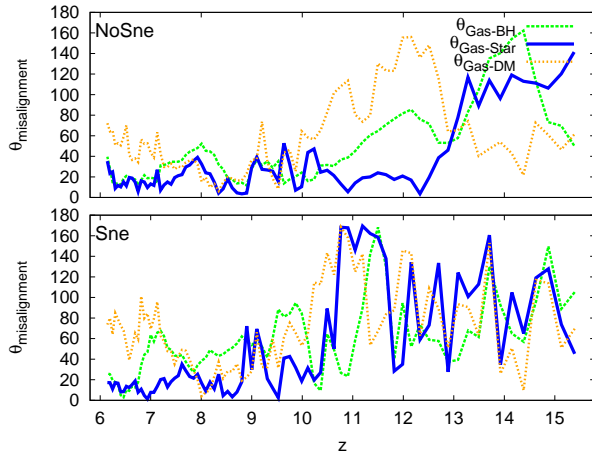


Figure 24. The misalignment angle between the gas spin and the BH spin in dashed green line, the gas spin and the stars in solid blue line and the gas spin and the DM spin in dotted orange line. NoSne run at the top panel and Sne run at the bottom panel. The gas and DM show a fluctuating misalignment angle with a high value at the end of the simulation. Due to the collisional nature of the gas it decouple from the DM once the pressure toques start to work on it. The gas, stars and BH finished the simulation well aligned but they suffer fluctuations on their angle due to mergers and SNe explosions.

initial growth of the proto-galaxy, but at low redshift they finished its evolution with a high degree of alignment. In the NoSne run the fluctuations in the angle evolution are related with pressure gradients associated to mergers suffered by the host halo, whereas in the Sne simulation beside the fluctuations associated to the mergers the extra source of misalignment are the SNe explosions.

The inclusion of AGN feedback in our simulation certainly could change both the galaxy and the BH evolution. The strong energy release on the gas can increase the gas temperature and may suppress the star formation. Furthermore, due to the outflows associated to the BH feedback the gas could not reach the central galactic region as easy as in the simulations presented here. A more detailed study about mass transport on high redshift galaxies with AGN feedback is left for a future work in preparation.

As a summary. In a cosmological context the galaxies are formed inside knots of the cosmic web surrounded by filaments. The gas flows from voids to the DM filaments from all directions. There the gas pile up in the filamentary structure and its pressure gradient cancels part of its angular momentum. The pressure torques dominate the filamentary structure whereas the gravitational torques have a non-dominant enhancement at the center of filaments. Part of the material inside the filaments formed by dense cold gas, flows onto the DM central halo in a almost free-fall due to the host DM halo gravitational attraction. The transported cold gas reaches the DM halo with a high radial component of the velocity producing strong pressure gradients at the edge of the galactic disc. The constant inflowing of cold gas creates a high gas fraction and cold environment at the inner $\sim 0.1R_{vir}$. Such a conditions promote a low Toomre parameter on the disc and then it becomes gravitationally unstable

forming very efficiently gas clumps which interact between them, with the galactic spiral arms and with merged DM haloes. Such a clumpy environment produce gravitational torque dominated regions on the disc, in other words the gravitational torque due to the VDI becomes an important source of MT. The other source of torques in our system is the pressure gradients. Due to the SNe explosions it complement the gravitational MT effect on this $z = 6$ galaxy. The mass accretion rate on the disc triggered by pressure and gravity fluctuates between $\sim 10^{-2} - 10^2 M_{\odot}/yr$ with an average around $\sim 1 M_{\odot}/yr$, which correspond to a $\sim 0.1\%$ of the large scale $\gtrsim R_{vir}$ mass accretion rate. Such a high mass accretion rates on the disc allow the central BH to grow substantially even in the presence of SNe explosions where $\langle f_{EDD} \rangle \sim 0.5$ in the z range from 15 to 6 ($\sim 0.6 Gyr$). This behavior allows a final BH mass of $\sim 6 \times 10^7 M_{\odot}$ at the end of the simulation.

ACKNOWLEDGMENTS

J.P. acknowledges the support from proyecto anillo de ciencia y tecnologia ACT1101. A.E. acknowledges partial support from the Center of Excellence in Astrophysics and Associated Technologies (PFB06), FONDECYT Regular Grant 1130458. Powered@NLHPC: This research was partially supported by the supercomputing infrastructure of the NLHPC (ECM-02). The Geryon cluster at the Centro de AstroIngenieria UC was extensively used for the analysis calculations performed in this paper. The Anillo ACT-86, FONDECYT EQUIP AIC-57 and QUIMAL 130008 provided funding for several improvements to the Geryon cluster. J.P. acknowledges the valuable comments and discussion from Yohan Dubois and Muhammad Latif. J.P. and A.E. acknowledge to Marta Volonteri for her enlightening comments on this work.

REFERENCES

- Abel T., Bryan G. L., & Norman M. L. 2002, *Science*, 295, 93
- Adams F. C., Ruden S. P., & Shu, F. H., 1989, *ApJ*, 347, 959
- Balbus S. A., 2003, *ARA&A*, 41, 555
- Begelman M. C. Volonteri, M. & Rees M. J. 2006, *MNRAS*, 370, 289
- Begelman M. C. Rossi E. M. & Armitage P. J. 2008, *MNRAS*, 387, 1649
- Bleuler A. & Teyssier R., 2014, *MNRAS*, 445, 4015
- Bondi H. & Lyttleton R. A., 1939, *Proceedings of the Cambridge Philosophical Society*, 35, 405
- Bondi H., 1952, *MNRAS*, 112, 195
- Booth C. M. & Schaye J., 2009, *MNRAS*, 398, 53
- Bournaud F., Elmegreen B. G. & Elmegreen D. M., 2007, *ApJ*, 670, 237
- Bromm V., & Larson R. B. 2004, *ARA&A*, 42, 79
- Bullock J. S., Kolatt T. S., Kravtsov A. V., Klypin A. A., Porciani C. & Primack J. R., 2001a, *ApJ*, 555, 240
- Codis S., Pichon C., Devriendt J., Slyz A., Pogosyan D., Dubois Y. & Sousbie T., 2012, *MNRAS*, 427, 3320

- Crain, R. A., Schaye, J., Bower, R. G., et al., 2015, MNRAS, 450, 1937
- Danovich M., Dekel A., Hahn O., Ceverino D. & Primack J., 2015, MNRAS, 449, 2087
- Devecchi B. & Volonteri M., 2009, ApJ, 694, 302
- Doroshkevich A. G., 1970, Afz, 6, 581
- Dubois Y., Pichon C., Haehnelt M., Kimm T., Slyz A., Devriendt J., & Pogosyan D., 2012, MNRAS, 423, 3616
- Dubois Y., Pichon C., Devriendt J., Silk J., Haehnelt M., Kimm T. & Slyz A., 2013, MNRAS, 428, 2885
- Dubois Y., Volonteri M., Silk J., Devriendt J. & Slyz A., 2014, MNRAS, 440, 2333
- Dubois Y., Volonteri M., Silk J., Devriendt J., Slyz A. & Teyssier R., 2015, MNRAS, 452, 1502
- Gammie Ch. F., 2001, ApJ, 553, 174
- Escala A., 2015, ApJ, 804, 54
- Escala A., 2007, ApJ, 671, 1264
- Escala A., 2006, ApJ, 648, 13
- Escala A. & Larson R. B., 2008, ApJ, 685L, 31E
- Fan X., et al., 2001, AJ, 121, 54
- Ferrarese L. & Merritt D., 2000, ApJ, 539, 9
- Ferrarese L. & Ford H., 2005, SSRv, 116, 523
- Fromang S., Balbus S. A., Terquem C. & De Villiers J., 2004, ApJ, 616, 364
- Ghez A. M., Salim S., Hornstein S. D., Tanner A., Lu J. R., Morris M., Becklin E. E. & Duchêne G., 2005, ApJ, 620, 744
- Gültekin K., Richstone D. O., Gebhardt K., Lauer T.R., Tremaine S., Aller M. C., Bender R., Dressler A., Faber S. M., Filippenko A. V., Green R., Ho L. C., Kormendy J., Magorrian J., Pinkney J. & Siopis C., 2009, ApJ, 698, 198
- Haardt F. & Madau P., 1996, ApJ, 461, 20
- Haiman, Z., 2013, ASSL, 396, 293
- Hartmann L., Calvet N., Gullbring E. & D'Alessio, P., 1998, ApJ, 495, 385
- Heger A., & Woosley S. E. 2002, ApJ, 567, 532
- Kennicutt R. C. Jr., 1998, ApJ, 498, 541
- Kimm T., Cen R., Devriendt J., Dubois Y. & Slyz A., 2015, MNRAS, 451, 2900
- Krumholz M. R., MaKee C. F. & Klein R. I., 2004, ApJ, 611, 399
- Krumholz M. R., Klein R. I. & MaKee C. F., 2007, ApJ, 659, 959
- Lodato G., Natarajan P., 2006, MNRAS, 371, 1813
- Mandelker N., Dekel A., Ceverino D., Tweed D., Moody C. E. & Primack J., 2014, MNRAS, 443, 3675
- Marconi A. & Hunt L. K., 2003, ApJ, 589L, 21
- McConnell N. J., Ma Ch., Gebhardt K., Wright Sh. A., Murphy J. D., Lauer T. R., Graham J. R. & Richstone D. O., 2011, Nature, 480, 215
- Nelson R. P. & Papaloizou J. C. B., 2003, MNRAS, 339, 983
- Oh S. P. & Haiman Z. 2002, ApJ, 569, 558
- Padoan P., Nordlund A., Kritsuk A. G., Norman M. L. & Li P. Sh., 2007, ApJ, 661, 972P
- Peebles P. J. E., 1969, ApJ, 155, 393
- Pichon C. & Bernardeau F., 1999, A&A, 343, 663
- Pichon C., Pogosyan D., Kimm, T., Slyz, A., Devriendt, J. & Dubois, Y., 2011, MNRAS, 418, 2493
- Planck Collaboration, 2013, arXiv:1303.5076P
- Powell L. C., Slyz A. & Devriendt J., 2011, MNRAS, 414, 3671
- Prieto J., Jimenez R., Haiman Z. & González R. E., 2015, MNRAS, 452, 784
- Prunet S., Pichon C., Aubert D., Pogosyan D., Teyssier R. & Gottloeber S., 2008, ApJs, 178, 179
- Rosas-Guevara, Y. M., Bower, R. G., Schaye, J., et al., 2013, arXiv:1312.0598
- Rosas-Guevara Y. M., Bower R. G., Schaye J., Furlong M., Frenk C. S., Booth C. M., Crain R. A., Dalla Vecchia C., Schaller M. & Theuns T., 2015, arXiv:1312.0598
- Shakura N. I. & Sunyaev R. A., 1973, A&A, 24, 337
- Shu F. H., Tremaine S., Adams F. C. & Ruden S. P., 1990, ApJ, 358, 495
- Schaye, J., Crain, R. A., Bower, R. G., et al. 2015, MNRAS, 446, 521
- Schneider R., Omukai K., Inoue A. K. & Ferrara A., 2006, MNRAS 369, 1437
- Starling R.L.C., Siemiginowska A., Uttley P. & Soria, R., 2004, MNRAS, 347, 67
- Sutherland R. S. & Dopita M. A., 1993, ApJ Sup., 88, 253
- Tanaka T., Haiman Z., 2009, ApJ, 696, 1798
- Teyssier R., 2002, A&A, 385, 337
- Teyssier R., Pontzen A., Dubois Y. & Read J. I., MNRAS, 429, 3068
- Toomre, A. 1964, ApJ, 139, 1217
- Tremaine S., Gebhardt K., Bender R., Bower G., Dressler A., Faber S. M., Filippenko A. V., Green R., Grillmair C., Ho L. C., Kormendy J., Lauer T. R., Magorrian J., Pinkney J. & Richstone D., 2002, ApJ, 574, 740
- Truelove J. K., Klein R. I., McKee Ch. F., Holliman J. H., Howell L. H. & Greenough J. A., 1997, ApJ, 489, 179
- Volonteri M., Lodato G., Natarajan P., 2008, MNRAS, 383, 1079
- Volonteri M., 2010, A&ARv, 18, 279

APPENDIX A

In order to compute the momentum flux in the \hat{r} direction due to processes in the $\hat{\theta}$ direction we projected the tensor F_{ik} in the $\hat{\theta}$ and then in \hat{r} direction:

$$F_{r\theta} = F_{ik}(\hat{x}^i \cdot \hat{\theta})(\hat{x}^k \cdot \hat{r}) \quad (42)$$

$$F_{r\theta} = [F_{xk}(\hat{x} \cdot \hat{\theta}) + F_{yk}(\hat{y} \cdot \hat{\theta})](\hat{x}^k \cdot \hat{r}) \quad (43)$$

$$F_{r\theta} = [F_{xx}(\hat{x} \cdot \hat{\theta})(\hat{x} \cdot \hat{r}) + F_{xy}(\hat{x} \cdot \hat{\theta})(\hat{y} \cdot \hat{r}) + F_{yx}(\hat{y} \cdot \hat{\theta})(\hat{x} \cdot \hat{r}) + F_{yy}(\hat{y} \cdot \hat{\theta})(\hat{y} \cdot \hat{r})] \quad (44)$$

$$F_{r\theta} = [-F_{xx} \sin \theta \cos \theta - F_{xy} \sin \theta \sin \theta + F_{yx} \cos \theta \cos \theta + F_{yy} \cos \theta \sin \theta] \quad (45)$$

$$F_{r\theta} = \frac{1}{2}(F_{yy} - F_{xx}) \sin 2\theta + F_{xy} \cos 2\theta, \quad (46)$$

We can do a similar exercise in order to compute the flux of \hat{z} AM in the \hat{r} direction due to stresses in the $\hat{\theta}$ direction, L_{rz} . In this case we project in the \hat{r} direction the \hat{z} component of the AM associated to the stresses in the $\hat{\theta}$ direction:

$$L_{rz} = \epsilon_{jmi} x_m F_{ik}(\hat{x}^j \cdot \hat{z})(\hat{x}^k \cdot \hat{r}) \quad (47)$$

$$L_{rz} = \epsilon_{zmi} x_m F_{ik} (\hat{x}^k \cdot \hat{r}) \quad (48)$$

$$L_{rz} = [\epsilon_{zmi} x_m F_{ix} (\hat{x} \cdot \hat{r}) + \epsilon_{zmi} x_m F_{iy} (\hat{y} \cdot \hat{r})] \quad (49)$$

$$L_{rz} = [\epsilon_{zyx} y F_{xx} (\hat{x} \cdot \hat{r}) + \epsilon_{zxy} x F_{yx} (\hat{x} \cdot \hat{r}) + \epsilon_{zyx} y F_{xy} (\hat{y} \cdot \hat{r}) + \epsilon_{zxy} x F_{yy} (\hat{y} \cdot \hat{r})] \quad (50)$$

$$L_{rz} = [-y F_{xx} + x F_{yx}] (\hat{x} \cdot \hat{r}) + [-y F_{xy} + x F_{yy}] (\hat{y} \cdot \hat{r}) \quad (51)$$

$$L_{rz} = (x F_{yx} - y F_{xx}) \cos \theta + (x F_{yy} - y F_{xy}) \sin \theta \quad (52)$$

Figure 25 shows the rate of angular momentum flux for our systems. The advantage of writing the above expressions is that both $F_{r\theta}$ and $L_{r,z}$ are easily computed in a grid based code.

APPENDIX B

Shakura & Sunyaev (1973) studied the MT process on a viscous disc. In such a model the MT is due to the effect of local viscous stresses. This process can be quantified by a rate of momentum flux term. This term can be written as a function of the viscosity ν and the velocity shears as follow:

$$S_{ik} = \rho \nu \left(\frac{\partial v_i}{\partial x_k} + \frac{\partial v_k}{\partial x_i} - \frac{2}{3} \delta_{ik} \nabla \cdot \vec{v} \right), \quad (53)$$

Assuming the strong constrain of a steady state of the momentum evolution, i.e. $\partial(\rho v_i)/\partial t = 0$, we obtain

$$\frac{\partial}{\partial x_k} (R_{ik} - S_{ik}) = 0. \quad (54)$$

In order to compute the MT in such a steady state, i.e. the term inside the partial derivative equal to a constant C , we can write the above equation as

$$R_{r\theta} = S_{r\theta} + C = \frac{3}{2} \alpha \rho c_s^2 + C \quad (55)$$

where we have parametrized the viscous tensor as a function of the α parameter. From this expression it is possible to compute an accretion rate assuming that the viscous term vanish at the inner edge of the disc, R_0 (which in general will be much shorter than our limit of resolution). After a z integration, assuming that the disc is rotating with a Keplerian velocity and using the expression for $S_{r\theta}$

$$S_{r\theta} = \rho \nu \{ [(\hat{r} \cdot \nabla) \vec{v}] \cdot \hat{\theta} + [(\hat{\theta} \cdot \nabla) \vec{v}] \cdot \hat{r} \} \quad (56)$$

we obtain

$$\Sigma v_r v_\theta = \Sigma \nu \Omega + C. \quad (57)$$

Denoting the disc angular velocity at the inner edge of the disc as $\Omega_0 = (GM/R_0)^{1/2}$ with M the mass of the central massive object we have

$$\Sigma v_r R_0 \Omega_0 = C, \quad (58)$$

and

$$\Sigma v_r r - \Sigma v_r R_0^{1/2} r^{1/2} = \Sigma \nu \quad (59)$$

$$\Sigma v_r r \left[1 - \left(\frac{R_0}{r} \right)^{1/2} \right] = \Sigma \nu \quad (60)$$

$$\dot{M} \left[1 - \left(\frac{R_0}{r} \right)^{1/2} \right] = 2\pi \Sigma \nu. \quad (61)$$

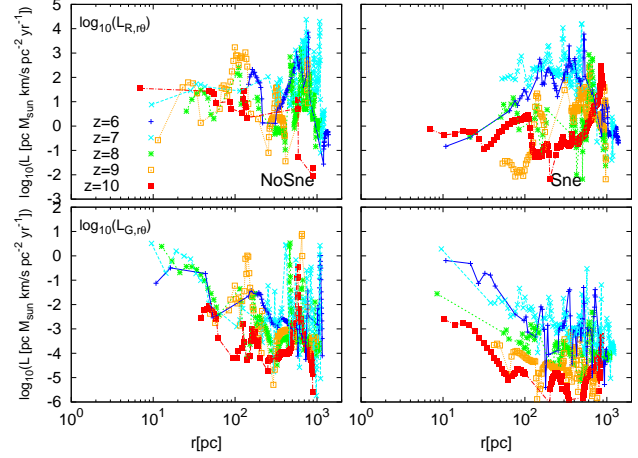


Figure 25. Same as 12 but for the rate of AM flux.

As mentioned above, in our case $R_0 \ll r$ and then the mass accretion rate can be approximated by

$$\dot{M} \approx 2\pi \Sigma \nu. \quad (62)$$

From the above equation and using the definition of the mass accretion rate it is possible to write $\nu = r v_r$ for this viscous MT model.

Assuming that the disc is supported by the gas pressure in the vertical direction and writing the viscosity as $\nu = 3\alpha L_{cs} c_s / 2$, with $L_{cs} = r c_s / v_\theta$ we have:

$$\begin{aligned} \dot{M} &= \frac{3\pi r \Sigma \alpha c_s^2}{v_\theta} \\ \dot{M} &= \frac{3\pi \Sigma \alpha c_s^2}{\Omega} \end{aligned} \quad (63)$$

Rearranging eq. 63 it is possible to compute an α parameter as a function of the mass accretion rate in this viscous model as (see figure 26):

$$\alpha = \frac{\dot{M} \Omega}{3\pi \Sigma c_s^2} \quad (64)$$

Now, using the definition of the mass accretion rate we can write

$$\begin{aligned} v_r &= \frac{3}{2} \frac{\alpha c_s^2}{v_\theta} \\ \alpha &= \frac{2}{3} \frac{v_r v_\theta}{c_s^2} \end{aligned} \quad (65)$$

$$\begin{aligned} \alpha &= \frac{2}{3} \frac{v_r}{v_\theta} \left(\frac{r}{L_{cs}} \right)^2 \\ \alpha &= \frac{1}{3\pi} \frac{t_{orb}}{t_{rad}} \left(\frac{r}{L_{cs}} \right)^2 \end{aligned} \quad (66)$$

We strength that the previous expressions for \dot{M} and α rise after to assume an stationary process for the momentum evolution, i.e. $\partial(\rho v_i)/\partial t = 0$. This implies that the term inside the divergence (the rate of momentum fluxes) should be a constant. In our case, as can be seen in fig. 12, such an assumption is not valid due to the highly dynamic nature of the system: hierarchical mass assembly producing DM halo mergers, non-isotropic accretion due to the filamentary

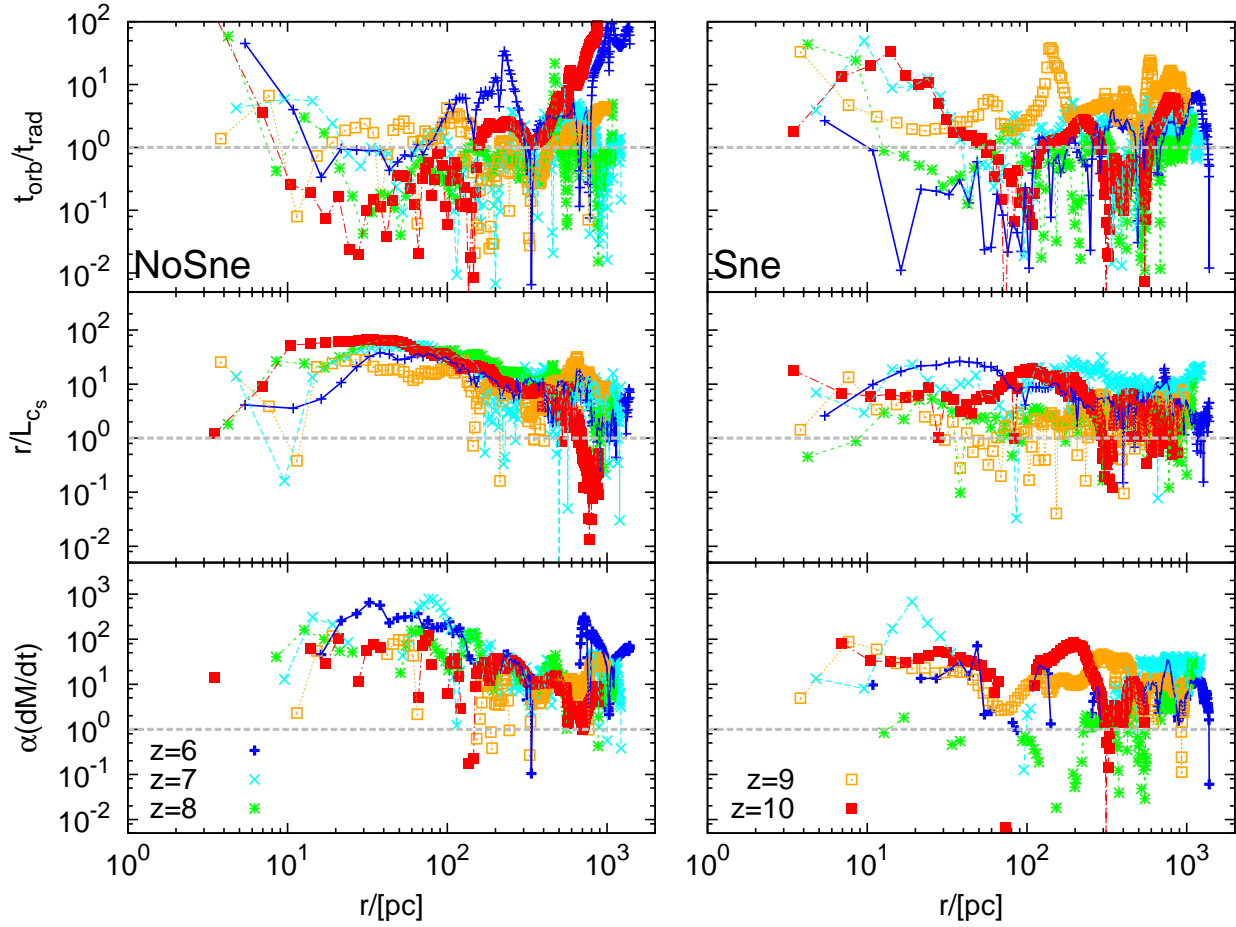


Figure 26. In the top row, the orbital to radial time as a function of radius for different redshifts. In the central, the radius to pressure height scale ratio. In the bottom row, the $\alpha_{r,\theta}$ parameter associated to the computed mass accretion rate in the simulations. From the top and the central panel we can deduce that the system has a non-stationary state with short radial times and a small pressure associated scale length. The final high α parameter reflects the non-stationary state of the system.

structure around the central DM halo and SNe explosions are working on the system.